Sede Amministrativa: Università degli Studi di Padova

Dipartimento di Biologia

CORSO DI DOTTORATO DI RICERCA IN: Bioscienze e Biotecnologie
CURRICOLO: Biochimica e Biofisica
CICLO 29°

Studying alterations of Ca^{2+} homeostasis in *in vitro* cell models of Amyotrophic Lateral Sclerosis

Coordinatore: Ch.mo Prof. Paolo Bernardi
Supervisore: Ch.mo Prof. Alessandro Bertoli

Dottorando : Rosa Pia Norante

INDEX

ABBREVIATIONS

$[Ca^{2+}]_{cyt}$	cytosolic free Ca^{2+} concentration
$[Ca^{2+}]_{er}$	ER Ca^{2+} concentration
$[Ca^{2+}]_{mit}$	mitochondrial free Ca^{2+} concentration
AEQ	Aequorin
AEQ_{cyt}	AEQ targeted to the cytosol
AEQ_{er}	AEQ targeted to the ER lumen
AEQ_{mit}	AEQ targeted to the mitochondrial matrix
AEQ_{pm}	AEQ targeted to the cytosolic domains proximal to the PM
ALS	Amyotrophic Lateral Sclerosis
AD	Alzheimer's disease
Aβ	amyloid beta peptide
AMPA	α-amino-3-hydroxy-5-methyl-4-isoxazole propionic acid
AMPA-R	AMPA-receptor
apoAEQ	apoprotetein AEQ
ATP	adenosine triphosphate
BSA	bovine serum albumin
Ca^{2+}	calcium ion
CFP	cyan fluorescent protein
CICR	Ca^{2+} induced-Ca^{2+} release
CNS	central nervous system
C9orf72	chromosome 9 open reading frame 72
DMSO	dimethylsulfoxide
EAAT2	excitatory amino acid transporter 2
ER	endoplasmic reticulum
f	familial

FCCP	trifluorocarbonylcyanide phenylhydrazone
FF	fast-fatigable
FRET	fluorescence (or Förster) resonance energy transfer
FTD	Frontotemporal Dementia
FUS/TLS	fused in sarcoma/translocated in liposarcoma
GECI	genetically encoded Ca^{2+} indicators
GFP	Green Fluorescent Protein
GluRs	glutamate receptors
HD	Huntington's disease
h	human
IP_3	inositol-1,4,5-trisphosphate
IP_3R	IP_3-sensitive receptor
KRB	Krebs-Ringer buffer
MCU	mitochondrial Ca^{2+} uniporter
MNs	motor neurons
mRFP	monomeric red fluorescent protein
mSOD1	mutant SOD1
NCX	Na^+/Ca^{2+} exchanger
NMDA	N-methyl-D-aspartate
NMDA-R	NMDA-receptor
P	polyclonal
PBS	phosphate buffer saline
PD	Parkinson's disease
PM	plasma membrane
PMCA	plasma membrane Ca^{2+} pump
PVDF	polyvinylidene fluoride
ROCC	receptor-operated Ca^{2+} channels

ROS	reactive oxygen species
RyR	ryanodine receptor
SDS	sodium dodecyl-sulphate
SERCA	sarco-endoplasmic reticulum Ca^{2+} pump
SOCC	store-operated Ca^{2+} channels
SOCE	store-operated Ca^{2+} entry
SOD1	superoxide dismutase 1
s	sporadic
STIM	stromal interaction molecules
TDP-43	TAR DNA-binding protein 43
TBS	Tris-buffered saline
TBS-T	Tris-buffered saline added with Tween-20
Tg	transgenic
TMRM	tetramethylrhodamine methyl ester probe
VGCC	voltage-gated Ca^{2+} channels
VOCC	voltage-operated Ca^{2+} channels
WB	Western blot
WT	wild type
YFP	yellow fluorescent protein
$\Delta\psi_m$	mitochondrial membrane potential

SUMMARY

Amyotrophic lateral sclerosis (ALS) is a fatal neurodegenerative disease characterized by the selective death of motor neurons (MNs). The mechanism of MN demise, however, is poorly understood, and no effective treatment is yet available. In most cases ALS occurs sporadically, but 10% of cases show a familial history and about 20% of these familial ALS (fALS) are caused by a mutation in the superoxide dismutase 1 (SOD1) gene. In particular, expression of the fALS-related SOD1(G93A) mutant in transgenic (Tg) mice closely resembles human disease. Recent research has found that mutant SOD1 (mSOD1) alters Ca^{2+} homeostasis in MNs and neighbouring astrocytes, thereby rendering MNs particularly vulnerable to the activation of a subset of harmful pathways. Such notions prompted us to compare local Ca^{2+} movements in spinal MNs and astrocytes from SOD1(G93A) and SOD1(WT) mice. To this purpose, we applied two different approaches.

1. Analysis of local Ca^{2+} fluxes in MNs.

i) We initially set the conditions for establishing MN-rich primary cultures from Tg mouse spinal cord;

ii) we engineered and produced adeno-associated viral (AAV) vectors for the expression of cameleon Ca^{2+} probes targeted to different cellular compartments, under the control of a MN-specific (Hb9-derived) promoter;

iii) we functionally tested and successfully used such Ca^{2+} probes for imaging Ca^{2+} oscillations in primary spinal cord MNs, demonstrating a specific expression in MNs and a higher Ca^{2+} entry in the cytosol through AMPA stimulation in SOD1(G93A) MNs compared to controls. We demonstrated also that this probes can also be expressed in vivo in spinal cord MNs upon systemic administration to newborn mice.

2. Analysis of local Ca^{2+} fluxes and related parameters in spinal astrocytes.

Following the notion that astrocytes affect disease progression in fALS Tg mice, we have also undertaken a thorough comparative investigation of local Ca^{2+} homeostasis in primary spinal astrocytes from SOD1(G93A) and SOD1(WT) mice to determine if mSOD1 impairs astrocyte Ca^{2+} homeostasis.

i) We initially set the conditions for the expression of locally targeted Ca^{2+} probes in primary spinal astrocytes;

(ii) following this approach, we provide evidence of altered Ca^{2+} homeostasis in different domains of SOD1(G93A) astrocytes following SOCE or exposure to ATP;

(iii) in the attempt to mechanistically explain the observed Ca^{2+} phenomenology, we have undertaken (by classical biochemical and immunocytochemical approaches) a thorough comparative analysis of the expression of major Ca^{2+}-transporting systems and other Ca^{2+}-related parameters in SOD1(G93A).

In conclusion our data emphasize that the expression of SOD1(G93A) is strictly correlated to altered Ca^{2+} homeostasis in spinal cord astrocytes, thereby supporting the hypothesis that in ALS astrocytes convey deadly signals to MNs through Ca^{2+}-dependent mechanisms.

RIASSUNTO

La sclerosi laterale amiotrofica (SLA) è una malattia neurodegenerativa fatale caratterizzata dalla morte selettiva dei motoneuroni (MN). Il meccanismo principe a cui è dovuto il danno neuronale è sconosciuto e non esiste un trattamento efficace per la cura di questa terribile malattia. In molti casi la SLA si sviluppa in maniera sporadica mentre nel 10% dei casi presenta una caratteristica genetica. Circa il 20% di questi casi famigliari sono causati da una mutazione nel gene della superossido dismutasi 1 (SOD1). In particolare, topi transgenici (Tg) esprimenti la mutazione SOD1 (G93A), correlata alla SLA, sviluppano un fenotipo molto simile a quello umano. Recenti ricerche hanno constatato come la proteina SOD1 mutata sia in grado di alterare l'omeostasi del calcio nei motoneuroni e negli astrociti limitrofi, rendendo le cellule neuronali particolarmente vulnerabili all'attivazione di un insieme di meccanismi possibilmente tossici. Considerando un tale stato dell'arte il nostro obiettivo, in questo progetto, è quello di confrontare flussi locali dello ione Ca^{2+} in motoneuroni e astrociti primari derivanti dal midollo spinale di topi SOD1(G93A) e SOD1(WT).

A questo scopo applicheremo due differenti approcci:

1. analisi dei flussi locali di Ca^{2+} in motoneuroni primari:

   i) abbiamo ottimizzate le condizioni di estrazione e messa in coltura di motoneuroni primari dal midollo spinale di topi Tg;

   ii) abbiamo ingegnerizzato e prodotto vettori virali adeno associati (AAV) per l'espressione delle sonde Ca^{2+} cameleon indirizzate a differenti compartimenti cellulari e sotto il controllo di un promotore motoneurone-specifico (derivato Hb9);

   iii) abbiamo testato funzionalmente e usato con successo le sonde per la misurazione delle variazioni di Ca^{2+} in MN spinali primari, dimostrando una espressione specifica della sonda nei MN e un alterato (incrementato) ingresso di Ca^{2+} nel citosol dopo stimolazione con AMPA nei MN SOD1(G93A) messi a confronto con il controllo. Abbiamo inoltre dimostrato che queste sonde possono essere espresse in vivo in MN del midollo spinale attraverso una somministrazione sistemica a topi neonati.

2. Analisi dei flussi locali di Ca^{2+} e dei relativi parametri in astrociti spinali primari

Considerando il noto effetto di cross-talk degli astrociti sui motoneuroni nel progredire della malattia in topi con fenotipo SLA, abbiamo intrapreso una analisi comparativa dei flussi locali di Ca^{2+} in astrociti spinali primari derivanti da topi SOD1(G93A) e SOD1(WT).

Al fine di determinare se la mutazione G93A fosse in grado di causare una variazione dell'omeostasi del Ca^{2+} si è proceduto nel seguente modo:

i) inizialmente abbiamo settato le condizione per l'espressione in astrociti spinali primari di sonde Ca^{2+} indirizzate a specifici compartimenti cellulari;

(ii) successivamente ci siamo focalizzati sulle misure di calcio fornendo la prova della presenza di flussi alterati di calcio in differenti domini cellulari di astrociti SOD1(G93A) dopo stimolazione del SOCE o recettori purinergici;

(iii) nel tentativo di ipotizzare un possibile pathway che spiegasse la fenomenologia osservata abbiamo intrapreso una analisi comparativa (attraverso tecniche classiche di biochimica e immunocitochimica), in astrociti spinali primari SOD1(WT) e SOD1(G93A), dell'espressione dei principali sistemi di trasporto dello ione Ca^{2+} e di altri parametri correlati.

Concludendo i nostri dati enfatizzano che l'espressione di SOD1(G93A) è strettamente correlata con una omeostasi alterata dello ione Ca2+ in astrociti derivanti da midollo spinale, tutto ciò avvalora ulteriormente l'ipotesi di un cross-talk letale tra astrociti e motoneuroni attraverso un meccanismo Ca^{2+} dipendente.

1. INTRODUCTION

1.1 Amyotrophic Lateral Sclerosis (ALS)

Amyotrophic Lateral Sclerosis (ALS), also known as Lou Gehrig's disease or Charcot disease, is a fatal neurodegenerative disorder, with a predominance 1.2-1.5/1 male/female[1], characterized by the selective loss of primary (cortical) and secondary (spinal) motor neurons (MNs). This selective death results in progressive weakness, difficulty in swallowing (dysphagia), breathing (dyspnea), atrophy of voluntary skeletal muscles, fasciculation and spasticity and in the end death. This neurodegenerative disorder is the most common amongst motor MN diseases and people of all races and ethnic background can be affected by ALS[2].

It's only after the early stage of axonal dysfunction and retraction that the neuronal cell body becomes visibly abnormal and dies, as has been shown in animal models. The exact timing of these events in human ALS is less certain, but the rare post-mortem reports on patients who died very early in the disease confirm this sequence[3].

It's known that 65% of general cases are classical (or spinal) forms where the firsts involved in the disease are limbs, while the remaining 35% are bulbar forms characterized by dysarthria and dysphagia. Usually the peak incidence of this disease is 50-70 years (juvenile ALS is rare) and the average age of death is 2-5 years after diagnosis[4]; in the majority of cases death occurs for denervation of the respiratory muscles and diaphragm[5].

Extensive studies carried out in recent years were not helpful to fully understand the mechanisms and the initial causes behind the neuronal degeneration that characterizes this disease. Indeed, despite intense effort, in literature and medicine no successful therapeutic strategy against this devastating disease are known, and as therapeutic option there is only a glutamate antagonist, benzothiazole riluzole, that increase survival of patients by few months slowing disease progression[6]. In the last few years, the understanding of some mechanisms of the disease underscored that ALS is probably part of a larger class of diseases, including Parkinson's disease, Frontotemporal Dementia (FTD) and ataxias[7–9].

ALS disease is divided in two main classes: sporadic (s) forms (without an obvious genetic component) and familial (f) forms, where the first covers 90% of the total cases and the second one the remainder 10%[10]. Nevertheless, in last years many defective genes were found to be associated to both sporadic and familial forms. Different factors can also define the age of onset, severity of the symptoms and the variability of clinical manifestations. For example, a recent study proposed a

mathematical model describing ALS as a multistep process closely related to six genetic and/or environmental factors[11].

Most is still unknown, however, on environmental factors in disease aetiology, though several studies have highlighted their possible involvement in ALS, especially in sporadic forms[12,13]. Pesticide contamination, heavy metals (e.g., lead) in toxic concentrations[14], smoking[15] and alcohol consumption, and viral and fungal infections have been associated to ALS pathogenesis[16]. Familial forms are characterized by the presence of genes with mostly classical pattern of inheritance.

The first gene, whose mutations were associated to fALS, was the one encoding superoxide dismutase 1 (SOD1) in 1993[17,18]. This was also the first gene enabling the generation of a transgenic (Tg) mouse model (expressing the ALS-related G93A mutant of human (h) SOD1) closely recapitulating different aspects of the pathologic phenotype of fALS and sALS[19]. The generation of such an animal model has fostered experimental research, and increased knowledge on basic disease mechanisms. Subsequently, several ALS-associated mutations were identified in other genes, including those coding for the TAR DNA-binding protein 43 (TDP-43), and the RNA-binding protein "fused in sarcoma/translocated in liposarcoma" (FUS/TLS)[20–22]. More recently, a close link between intronic hexanucleotide (GC) repeat expansions in the chromosome 9 open reading frame 72 (*C9orf72*) gene and both fALS and sALS has been established[23,24].

Together, the 4 genes described above account 60-80% of fALS cases. In particular mutations in *C9orf72* cover most of familial form and the disease appears after the age of 40, while mutations in FUS/TLS are found in 10% of familial cases appearing before 40 years of age[25] (Fig.1).

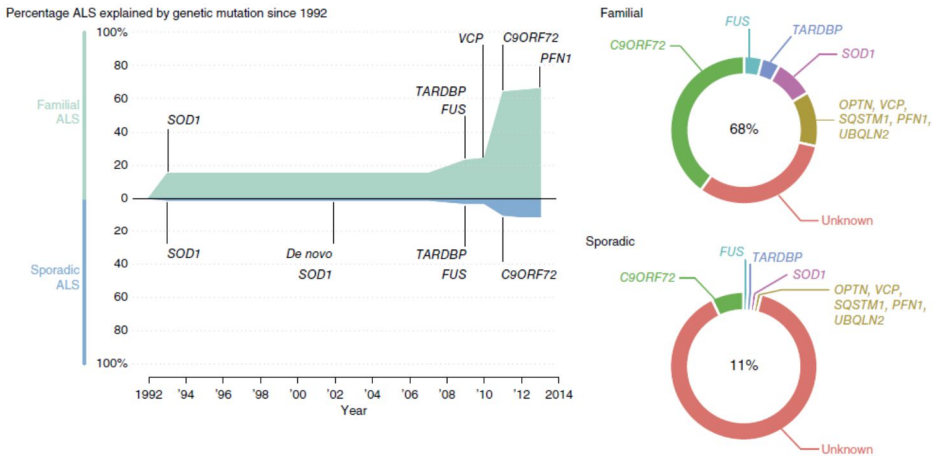

Fig. 1 Timeline of gene discoveries in familial and sporadic ALS. Values represent the proportion of ALS explained by each gene in populations of European ancestry[26].

All these genes, and the relative encoded proteins, take part to a very heterogeneous set of cell pathways, among which DNA/RNA processing, autophagy, vesicles transport, energy metabolism, cytoskeletal dynamics, apoptosis, oxidative stress scavenging, mitochondrial integrity, and more[27] (Fig. 2).

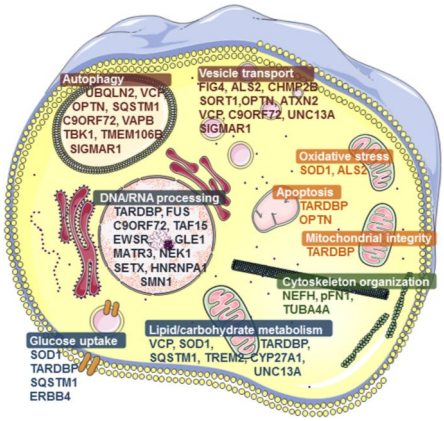

Fig. 2 Main cellular functions where ALS causative or susceptibility genes are involved[27].

In spite of this heterogeneity of mechanisms, the symptoms and the progression of the illness are similar between the familial and sporadic forms of ALS.

1.2 Superoxide dismutase 1 (SOD1)

SOD1 is a ubiquitous, predominantly cytosolic protein of 153 amino acids. It is an homo-dimeric Cu/Zn-binding enzyme (32KDa) encoded by the SOD1 gene, located on the chromosome 21, and composed of eight antiparallel β-barrels containing an intramolecular disulphide bond and a binuclear Cu/Zn site in each subunit (Fig.3).

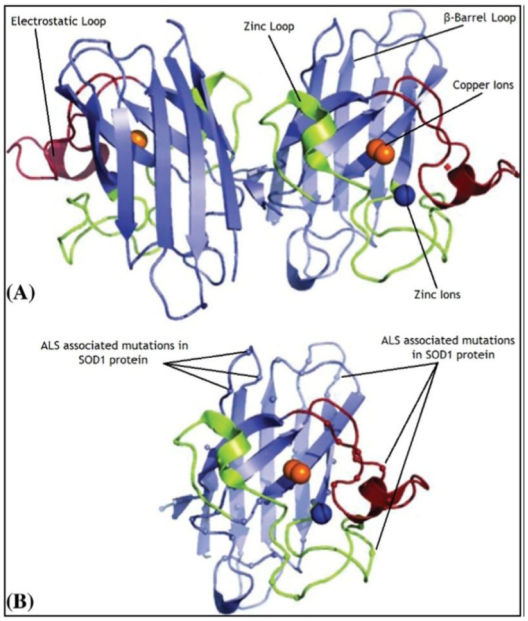

Fig. 3 A) Structure of human SOD1 protein. The beta barrel, the zinc loop and the electrostatic loop are shown in blue, green and red colour, respectively. The copper and zinc ions are shown as orange and blue spheres, respectively. B) ALS-related mutations in the SOD1 protein. The SOD1 mutations are shown as small spheres within the SOD1 protein monomer[28].

This protein is widely expressed and constitutes about 0.5/0.8% of soluble proteins in the brain. Its task is to catalyse the conversion of the superoxide anion in hydrogen peroxide and dioxygen through cyclic reduction and oxidation (dismutation) of Cu^{2+} to protect cells from reactive oxygen species (ROS) toxicity[29]. Mature protein is highly stable, but when it is in the metal-free and in disulphide-reduced form, SOD1 dysfunctions and tendency to oligomerization and aggregation is observed[30,31].

Approximately 10% of fALS and 3% of sALS cases are related to SOD1 mutations[32–34]. More than 150 SOD1 mutations have been identified in ALS[34], most of which are missense (involving at least 75 aminoacids), while 12 mutations are nonsense or deletion mutations that produce truncated proteins. Among all fALS-associated mutations in the hSOD1 gene, the most common are G93A (that is also the most studied), A4V (the most prevalent (50%) in USA), H46R (the most prevalent in Japan), and D90A that represents 50% of fALS cases in Sweden and Finland[28].

In Tg rodent models and human ALS cases SOD1-immunoreactive aggregates are evident by the time of disease onset and increase over time. Mutant SOD1 (mSOD1) displays also prion-like properties *in vitro* and in animal models as demonstrated by the evidence that mSOD1 has the ability to sequester wild-type (WT) proteins and seed their aggregation or misfolding acting as transmissible agents between cells (mSOD1 are found in medium from primary cultures of astrocyte)[35]. Moreover, selective expression of mSOD1 in MNs, astrocytes and microglia *in vivo* indicated that interaction between these cells is necessary to lead to MN degeneration and to the ALS typical phenotype, showing that MNs death is not cell autonomous[36–40].

Many lines of evidence have led to the conclusion that mutations in this protein cause ALS via an as yet unidentified toxic gain of function. Indeed, perturbations of different cellular systems have been implicated in ALS, but the correlation between the enzymatic activity of SOD1 and the clinical progression and disease phenotype is not yet clear. Moreover, the duration of the disease is similar for any given mutations[32].

mSOD1 impairs multiple cellular functions, including endoplasmic reticulum (ER) stress and Ca^{2+} overload, sensitizing MNs to apoptosis. Moreover, MNs of mSOD1 mice show early abnormalities in mitochondrial structure and physiology, such as dilated cristae and mitochondrial swelling, reduction in electron transport chain activity (especially in complex I and IV), reduced respiratory rate, mitochondrial membrane potential ($\Delta\psi_m$) and adenosine triphosphate (ATP) generation. There is also *in vivo* evidence (based on the analysis of the cerebrospinal fluid of ALS patients) for excitotoxicity generated by excessive stimulation of postsynaptic glutamate receptors[41–45].

The most exploited mouse model of ALS is that based on Tg mice expressing the hSOD1(G93A) missense mutant. Mice hemizygous for hSOD1(G93A) transgene are viable and fertile, and exhibit a phenotype similar to human ALS: they become paralyzed in one or more limbs due to loss of MNs from the spinal cord. Tg mice have an abbreviated life span: 50% survive at 128.9+/-9.1 days.

1.3 Ca^{2+} homeostasis and neurodegenerative disorders

The calcium ion (Ca^{2+}) is the major intracellular messenger, mediating a variety of physiological responses to chemical and electrical stimulations. Therefore, cell Ca^{2+} concentrations must be tightly controlled in terms of both space and time, a task that is accomplished by several Ca^{2+} transporting and buffering systems.

Excitable cells, and neurons in particular, are highly sensitive to subtle and transient rises of cellular Ca^{2+} concentrations that are primarily mediated by voltage-operated Ca^{2+} channels (VOCC) and receptor-operated Ca^{2+} channels (ROCC) of the plasma membrane (PM). Among the latter ones, ionotropic receptor channels for glutamate (a major excitatory neurotransmitter), including N-methyl-D-aspartate (NMDA) and α-amino-3-hydroxy-5-methyl-4-isoxazolepropionic acid (AMPA) receptors, are particularly important for excitatory neurons in the central nervous system. Also the release of Ca^{2+} from the ER, by the activation of G-protein-coupled metabotropic glutamate receptors that stimulates the production of inositol trisphosphate (IP_3) and downstream activation of Ca^{2+} channels in the ER (IP_3- and ryanodine-receptors), is crucial for Ca^{2+} metabolism. In parallel, the coordinated action of different extrusion systems, including the PM Na^+/Ca^{2+} exchanger (NCX), and the PM- and sarco/endoplasmic reticulum-Ca^{2+} ATPases (PMCA and SERCA, respectively) ensures a fine and timely control of the cytosolic Ca^{2+} concentration (Fig. 4).

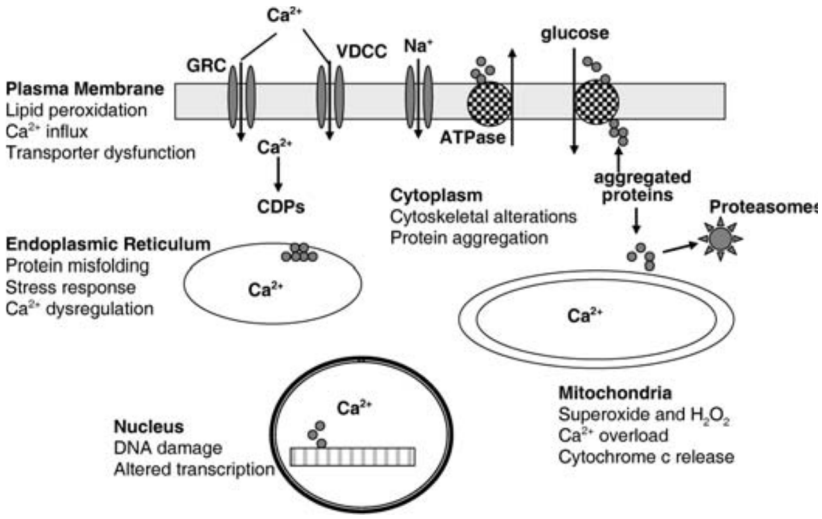

Fig 4. Subcellular systems involved in the disruption of neuronal Ca^{2+} homeostasis in aging and neurodegenerative disorders. Oxidative stress causes peroxidation of lipids in the plasma membrane that impairs the function of ion-motive ATPases and glucose transporter proteins. This promotes membrane depolarization and cellular energy depletion, which results in excessive Ca^{2+} influx and accumulation of Ca^{2+} within the cell. Perturbed Ca^{2+} homeostasis may also result from endoplasmic reticulum stress and mitochondrial dysfunction. Abnormal aggregation of proteins contribute to the damage and dysfunction of Ca^{2+}-regulating systems. Excessive amounts of Ca^{2+} within the neuron can cause dysfunction of a myriad of cellular processes. Calcium dependent proteases (CDPs)[46].

In light of the above concepts, it is not surprising that Ca^{2+} metabolism plays a critical role in different fundamental functions of neurons, such as synaptic transmission, neurite outgrowth and synaptogenesis, neuronal plasticity, short- and long-term memory and cell survival. Accordingly, it is not surprising that perturbed Ca^{2+} homeostasis is detrimental to neuronal activity and survival. Indeed, a close link between the pathogenesis of different neurodegenerative disorders and Ca^{2+} regulating systems, the so called *"calcium hypothesis of neurodegenerative diseases"*, has been convincingly forwarded by several experimental findings[46,47].

Different cellular perturbations as oxidative stress, perturbed energy metabolisms and aggregation of disease-related proteins can affect Ca^{2+} homeostasis. Dysfunctions of Ca^{2+}-regulating proteins in PM, ER and mitochondria are involved in age-related neuronal diseases. The effects of aging on neuronal Ca^{2+} concentrations can be genetic or due to environmental factors that increase the risk of neurodegenerative disorders[46]. For example, age-related accumulation of ROS and perturbed cellular metabolisms, such as reduced mitochondrial functions, result in aberrant Ca^{2+} metabolism in different cell compartments, and are strictly associated with normal aging in most tissues, and also implicated in major neurodegenerative disorders[48,49].

Mitochondria are the major source of ATP, but also of ROS, in neurons. Therefore, alterations of Ca^{2+}-dependent mitochondrial functions play a pivotal role in neuronal damage during aging or disease, including Alzheimer's disease (AD), Parkinson's disease (PD), Huntington's disease (HD) and ALS[47]. Accordingly, analysis of brain tissues have shown alterations of Ca^{2+} homeostasis during the progression of different neurodegenerative disorders. For example, the AD-related amyloid beta (Aβ) peptide disrupts neuronal Ca^{2+} homeostasis, possibly via ROS production. This peptide (directly – by forming Ca^{2+}-permeable pores in the PM – or indirectly) is also involved in the elevation of basal intracellular Ca^{2+} levels, which sensitize neurons to excitotoxicity and apoptosis[46,49].

Also in Amyotrophic Lateral Sclerosis there are many evidences of the correlation between protein misfolding and Ca^{2+} homeostasis. In fact recent research has found that mSOD1 alters Ca^{2+} homeostasis in MNs, and renders MNs particularly vulnerable to the activation of a subset of harmful pathways[50,51]. This could be the case, for example, of cytotoxic Ca^{2+} overloads, in light of the finding that fALS MNs exhibit abnormal Ca^{2+} levels in the cytosol and other cell compartments[52–55]. On the other hand, can also be assumed that ER and mitochondrial Ca^{2+} mishandling generates ER stress and mitochondrial dysfunctions, which have been causally linked to the disease. In addition, it has been recently provided evidence that the inherent excitability of MNs can act as an early endogenous neuroprotective mediator in mouse models of mSOD1 fALS,

suggesting that reduced excitability may be causally linked to the early progression of disease, in particular in the ALS-vulnerable "fast-fatigable" (FF) MN subset[56]. Given that Ca^{2+} is closely linked to neuronal excitability, it is likely that mutant SOD1-induced derangements of MN Ca^{2+} control are involved in the loss, or weakening, of neuroprotective pathways.

Within the tenets of the Ca^{2+} hypothesis of neurodegenerative diseases, deregulation of Ca^{2+} signalling is one of the early events and key processes in disease pathogenesis. Of consequence, different approaches have been applied to protect or restore normal Ca^{2+} homeostasis in neurons, in order to prevent or delay Ca^{2+} overload and neuronal degeneration in acute and chronic neurodegenerative conditions[57,58]. Examples are drugs that suppress Ca^{2+} influxes, which – unfortunately – have the adverse effect to compromise normal neuronal functions in long-term treatment[46].

In summary, a better understanding of how derangements of Ca^{2+} fluxes promote neuronal demise in aging and neurodegenerative disorder may help identifying novel targets and strategies for neuroprotective therapeutic interventions[49].

1.4 Astrocyte-MN cross-talk and its relevance to ALS

The precise molecular mechanism(s) that target MNs to death in ALS still remain elusive, nor there are effective therapies that prevent or slow down disease progression. For this reason, a better understanding of ALS pathogenic mechanisms is very important to ameliorate the disease onset and progression.

The long-standing view that MNs were the sole target of ALS and that MN damage occurred through cell autonomous pathways has been recently questioned by the idea that other cell types, such as glial cells and skeletal myocytes, contribute by *in-trans* (non-cell autonomous) mechanisms to MN demise. In addition, it is now largely accepted that astrocytes have both structural and functional interactions with neighbouring neurons, and are actively involved in synaptic transmission, forwarding the concept of "tripartite synapse" that involves pre-and post-synaptic neuronal terminals and adjacent astrocytes (Fig.5)[59].

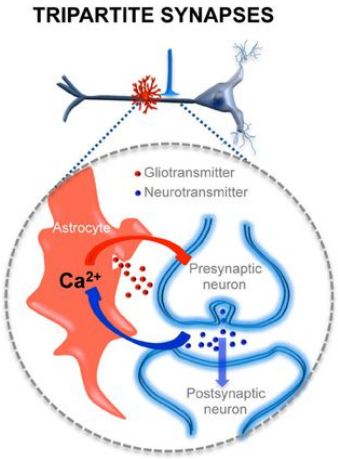

Fig. 5 Structural and functional relationships of neurons and astrocytes and tripartite synapses. Scheme of one axon establishing a synapse on an apical dendrite of a prototypical pyramidal neuron and an astrocyte located close to it (in red). The large dashed circle illustrates an enlarged schematic view of the tripartite synapse, where the pre- and postsynaptic neuronal elements (in blue) are surrounded by astrocytic processes (in red). It also depicts the transfer of information between neuronal synaptic elements and astrocytic processes. Astrocytes respond with Ca^{2+} elevations to neurotransmitters (blue dots) released during synaptic activity and, in turn, control neuronal excitability and synaptic transmission through the Ca^{2+} -dependent release of gliotransmitters (red dots)[59].

Unlike neurons, astrocytes are not "electrically" active, but, nevertheless, they display "excitable" responses based on rapid and transient variations of the intracellular Ca^{2+} content. Such Ca^{2+} oscillations are key to regulate a broad variety of astrocytic functions, including the release of gliotransmitters that are relevant for astrocyte-to-neuron communication. Accordingly, altered astrocyte signalling has been suggested to contribute – through non-cell autonomous processes – to neuronal dysfunctions in different neurodegenerative disorders, including ALS[38,60]. For example, the silencing of mSOD1 expression in astrocytes slows disease progression in fALS Tg mice in

vivo[60], while the specific expression of mSOD1 and mTDP-43 in astrocytes disrupts MN mitochondrial functions in primary astrocyte/MN co-culture models[36].

Furthermore, one of the major pathological feature of ALS is the activation and migration of astrocytes within and around the damaged regions of the spinal cord. This proliferation and adoption of a reactive phenotype is due to the response of astrocytes to cellular stresses[61]. During this neuroinflammation process, astrocytes become neurotoxic by losing their normal support and trophic function towards MNs, and secreting cytotoxic cytokines[62].

Another important aspect is that in normal conditions astrocytes are involved in the clearance of glutamate from the synaptic cleft to prevent neuronal excitoxicity due to glutamate overexposure. In ALS, however the expression of the excitatory amino acid transporter 2 (EAAT2), the major mechanism for glutamate uptake in astrocytes, is significantly decreased, resulting in MN excitotoxicity, both in the spinal cord of ALS patients[63], and in animal models[64].

Astrocytes are also able to release factors selectively toxic to MN[65,66], playing a role in the specific degeneration of spinal MNs in ALS. Important is also the finding implicating Ca^{2+} dysomeostasis of hSOD1(G93A)-expressing astrocytes (with release of neurotoxic factors) in MN degeneration[66–68].

1.5 Genetically encoded Ca^{2+} indicators

Ca^{2+} imaging is an increasingly used technical approach in cell biology to map intracellular Ca^{2+} signalling by measuring time- and space-resolved fluctuations of the ion concentration. This approach takes advantage of both chemical probes and genetically encoded Ca^{2+} indicators (GECI). The latter ones are fluorescent or luminescent Ca^{2+}-sensitive proteins that are not toxic to cells and can be genetically targeted – by fusion to suitable signal peptide sequences – to specific cell organelles/compartments. Such probes can be efficiently transduced into living cells using different expression systems.

Aequorin (AEQ) is a calcium-binding bio-luminescent protein produced by the jellyfish *Aequorea victoria*. This protein was isolated and characterized in the early sixties of the last century by Osamu Shimomura and colleagues[69], but the first attempts to detect Ca^{2+} fluxes by AEQ date to the early seventies[70]. Thanks to the engineering of chimeric constructs containing specific targeting sequences, this photo-protein virtually allows the analysis of Ca^{2+} concentrations and dynamics in all cell compartments, including cytosol, cytosolic domains proximal to the PM, mitochondrial matrix and ER lumen. The advantages of using this kind of probe include the selective intracellular distribution, low background (and – consequently – high signal-to-noise ratio)and the possibility to introduce mutations in the Ca^{2+}-sites for providing a wide dynamic range of K_d for Ca^{2+} binding[71,72]. Given the low luminescent AEQ signal that requires cell population measurements, disadvantages of such a probe are principally related to the difficulty of obtaining sufficiently high rate of transduction in some cell preparations. This problem can be circumvented by use of (lenti)viral expression vectors[73].

AEQ is composed by an apoprotein (apoAEQ) with an approximate molecular weight of 21 kDa, and the prosthetic group coelenterazine (luciferin). apoAEQ contains three Ca^{2+}-binding EF hand motifs that, upon cooperative Ca^{2+} binding, impart conformational changes promoting oxidative conversion of coelenterazine to coelenteramide and concomitant emission of light (λ = 469 nm) [73] (Fig. 6).

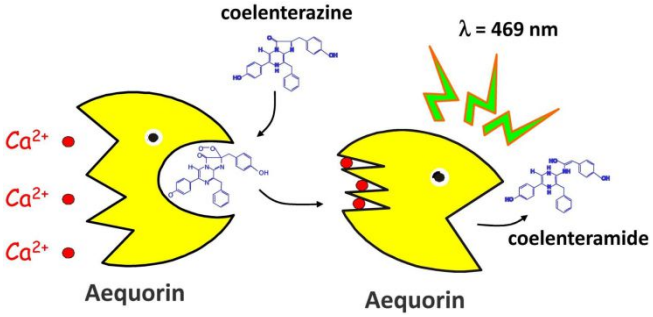

Fig. 6 AEQ contains three Ca^{2+}-binding domains. When non-covalently bound to its prosthetic group coelenterazine, AEQ binds to three Ca^{2+} ions catalysing the oxidation of coelenterazine into coelenteramide. The reaction is accompanied by emission of blue light (λ = 469 nm).

Cameleon probes are based on fluorescence (or Förster) resonance energy transfer (FRET), a well-known quantum mechanical process consisting in the non-radiating energy transfer from an exited fluorescent donor to an acceptor fluorophore placed in close proximity. Therefore, when FRET occurs, an increased fluorescence of the acceptor, together with a decreased fluorescence of the donor can be observed, and quantified as the ratio between the two fluorescent signals. To date, the most used GFP-modified proteins in cameleons are the cyan fluorescent protein (CFP, acting as donor) and the yellow fluorescent protein (YFP, acceptor) (Fig. 7).

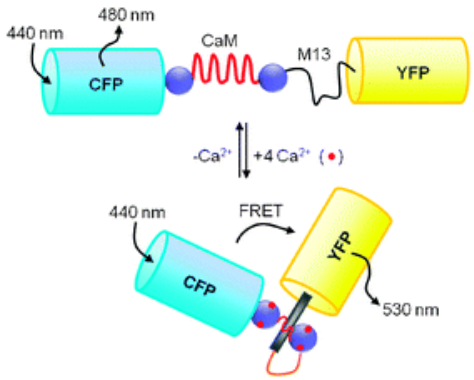

Fig. 7 In cameleons the donor and the acceptor are both derived from the green fluorescent protein (GFP, isolated from *Aequorea victoria*), and are separated – in a chimeric construct – by a Ca^{2+}-sensing peptide consisting of calmodulin (CaM) and a CaM-binding peptide derived from the myosin light chain kinase M13 (M13), separated by a glycyl-glycine linker. While in the absence of Ca^{2+} (or the presence of low Ca^{2+} concentrations) the CaM/M13 domain presents in an extended form, when this Ca^{2+}-sensing domain binds Ca^{2+} ions it forms a packed globular structure that brings the FRET donor and acceptor in close spatial proximity, thereby allowing FRET to occur.

In last years, site-directed mutagenesis provided researcher with improved cameleon probes that possess increased brightness of the FRET acceptor, reduced competitive binding to endogenous CaM, and larger K_d range for Ca^{2+} binding rendering such probes suitable for Ca^{2+} measurements in different cell districts, and under different conditions (e.g., basal Ca^{2+} levels, or Ca^{2+} transients upon cell stimulation)[74,75].

Transduction of genetic materials into target cells using viral infection often represents the unique solution with primary cultures. A number of different viral expression systems have been developed, including lentivirus-, adenovirus- and adeno-associated virus-based vectors. Each of this viral vectors has different characteristics and is suitable for different cell models and experimental settings (vigenebio.com).

In particular, in our project adeno-associated virus are used for cameleon probes while aequorin photo-protein is expressed in primary spinal astrocytes using lentiviral strategy.

2. BIBLIOGRAFY

1. Logroscino, G. *et al.* Incidence of amyotrophic lateral sclerosis in Europe. *J. Neurol. Neurosurg. Psychiatry* **81,** 385–90 (2010).

2. Hardiman, O., van den Berg, L. H. & Kiernan, M. C. Clinical diagnosis and management of amyotrophic lateral sclerosis. *Nat. Rev. Neurol.* **7,** 639–649 (2011).

3. Robberecht, W. & Philips, T. The changing scene of amyotrophic lateral sclerosis. *Nat. Rev. Neurosci.* **14,** 1–17 (2013).

4. Shaw, C. E., al-Chalabi, a & Leigh, N. Progress in the pathogenesis of amyotrophic lateral sclerosis. *Curr. Neurol. Neurosci. Rep.* **1,** 69–76 (2001).

5. Kiernan, M. C. *et al.* Amyotrophic lateral sclerosis. *Lancet* **377,** 942–955 (2011).

6. Yáñez, M. *et al.* The neuroprotection exerted by memantine, minocycline and lithium, against neurotoxicity of CSF from patients with amyotrophic lateral sclerosis, is antagonized by riluzole. *Neurodegener. Dis.* **13,** 171–179 (2014).

7. Strong, M. J. The syndromes of frontotemporal dysfunction in amyotrophic lateral sclerosis. *Amyotroph. Lateral Scler.* **9,** 323–338 (2008).

8. Pradat, P.-F. *et al.* Extrapyramidal stiffness in patients with amyotrophic lateral sclerosis. *Mov Disord* **24,** 2143–8 (2009).

9. Mackenzie, I. R. A., Rademakers, R. & Neumann, M. TDP-43 and FUS in amyotrophic lateral sclerosis and frontotemporal dementia. *The Lancet Neurology* **9,** 995–1007 (2010).

10. Rowland, L. & Shneider, N. Amyotrophic Lateral Sclerosis. *N. Engl. J. Med.* **344,** 1688–1700 (2001).

11. Al-Chalabi, A. *et al.* Analysis of amyotrophic lateral sclerosis as a multistep process: A population-based modelling study. *Lancet Neurol.* **13,** 1108–1113 (2014).

12. Al-Chalabi, A. & Hardiman, O. The epidemiology of ALS: a conspiracy of genes, environment and time. *Nat. Rev. Neurol.* **9,** 617–28 (2013).

13. Ingre, C., Roos, P. M., Piehl, F., Kamel, F. & Fang, F. Risk factors for amyotrophic lateral sclerosis. *Clinical Epidemiology* **7,** 181–193 (2015).

14. Kamel, F. *et al.* Amyotrophic lateral sclerosis, lead, and genetic susceptibility: polymorphisms in the delta-aminolevulinic acid dehydratase and vitamin D receptor genes. *Environ. Health Perspect.* **111,** 1335–9 (2003).

15. Armon, C. Smoking may be considered an established risk factor for sporadic ALS. *Neurology* **73,** 1693–1698 (2009).

16. Trojsi, F., Monsurr??, M. R. & Tedeschi, G. Exposure to environmental toxicants and pathogenesis of amyotrophic lateral sclerosis: State of the art and research perspectives. *International Journal of Molecular Sciences* **14,** 15286–15311 (2013).

17. Deng, H. X. *et al.* Amyotrophic lateral sclerosis and structural defects in Cu,Zn superoxide dismutase. *Science* **261,** 1047–1051 (1993).

18. Rosen, D. R. *et al.* Mutations in Cu/Zn superoxide dismutase gene are associated with familial amyotrophic lateral sclerosis. *Nature* **362,** 59–62 (1993).

19. Gurney, M. E. *et al.* Motor neuron degeneration in mice that express a human Cu,Zn superoxide dismutase mutation. *Science* **264,** 1772–5 (1994).

20. Neumann, M. *et al.* Ubiquitinated TDP-43 in frontotemporal lobar degeneration and amyotrophic lateral sclerosis. *Science* **314,** 130–3 (2006).

21. Neumann, M. *et al.* A new subtype of frontotemporal lobar degeneration with FUS pathology. *Brain* **132,** 2922–2931 (2009).

22. Vance, C. *et al.* Mutations in FUS, an RNA Processing Protein, Cause Familial Amyotrophic Lateral Sclerosis Type 6. *Science (80-.).* **323,** 1208–1211 (2009).

23. DeJesus-Hernandez, M. *et al.* Expanded GGGGCC Hexanucleotide Repeat in Noncoding Region of C9ORF72 Causes Chromosome 9p-Linked FTD and ALS. *Neuron* **72,** 245–256 (2011).

24. Renton, A. E. *et al.* A hexanucleotide repeat expansion in C9ORF72 is the cause of chromosome 9p21-linked ALS-FTD. *Neuron* **72,** 257–268 (2011).

25. Millecamps, S. *et al.* Phenotype difference between ALS patients with expanded repeats in C9ORF72 and patients with mutations in other ALS-related genes. *J. Med. Genet.* **49,** 258–263 (2012).

26. Renton, A. E., Chiò, A. & Traynor, B. J. State of play in amyotrophic lateral sclerosis genetics. *Nat. Neurosci.* **17,** 17–23 (2014).

27. Zufiría, M. *et al.* ALS: A bucket of genes, environment, metabolism and unknown ingredients. *Prog. Neurobiol.* **142,** 104–129 (2016).

28. Kaur, S. J., McKeown, S. R. & Rashid, S. Mutant SOD1 mediated pathogenesis of Amyotrophic Lateral Sclerosis. *Gene* **577,** 109–118 (2016).

29. Reddi, A. R. & Culotta, V. C. SOD1 integrates signals from oxygen and glucose to repress

respiration. *Cell* **152,** 224–235 (2013).

30. Bruijn, L. I. *et al.* Aggregation and motor neuron toxicity of an ALS-linked SOD1 mutant independent from wild-type SOD1. *Science* **281,** 1851–1854 (1998).

31. Saccon, R. A., Bunton-Stasyshyn, R. K. A., Fisher, E. M. C. & Fratta, P. Is SOD1 loss of function involved in amyotrophic lateral sclerosis? *Brain* **136,** 2342–2358 (2013).

32. Pasinelli, P. & Brown, R. H. Molecular biology of amyotrophic lateral sclerosis: insights from genetics. *Nat. Rev. Neurosci.* **7,** 710–723 (2006).

33. Acevedo-Arozena, A. *et al.* A comprehensive assessment of the SOD1G93A low-copy transgenic mouse, which models human amyotrophic lateral sclerosis. *Dis. Model. Mech.* **4,** 686–700 (2011).

34. Andersen, P. M. & Al-Chalabi, A. Clinical genetics of amyotrophic lateral sclerosis: what do we really know? *Nat Rev Neurol* **7,** 603–615 (2011).

35. Basso, M. *et al.* Mutant copper-zinc superoxide dismutase (SOD1) induces protein secretion pathway alterations and exosome release in astrocytes: Implications for disease spreading and motor neuron pathology in amyotrophic lateral sclerosis. *J. Biol. Chem.* **288,** 15699–15711 (2013).

36. Bilsland, L. G., Nirmalananthan, N., Yip, J., Greensmith, L. & Duchen, M. R. Expression of mutant SOD1G93A in astrocytes induces functional deficits in motoneuron mitochondria. *J. Neurochem.* **107,** 1271–1283 (2008).

37. Nagai, M. *et al.* Astrocytes expressing ALS-linked mutated SOD1 release factors selectively toxic to motor neurons. *Nat. Neurosci.* **10,** 615–22 (2007).

38. Boillée, S., Vande Velde, C. & Cleveland, D. W. ALS: A Disease of Motor Neurons and Their Nonneuronal Neighbors. *Neuron* **52,** 39–59 (2006).

39. Vande Velde, C., Miller, T. M., Cashman, N. R. & Cleveland, D. W. Selective association of misfolded ALS-linked mutant SOD1 with the cytoplasmic face of mitochondria. *Proc. Natl. Acad. Sci. U. S. A.* **105,** 4022–7 (2008).

40. Di Giorgio, F. P., Carrasco, M. A., Siao, M. C., Maniatis, T. & Eggan, K. Non-cell autonomous effect of glia on motor neurons in an embryonic stem cell-based ALS model. *Nat. Neurosci.* **10,** 608–14 (2007).

41. Cozzolino, M. & Carri, M. T. Mitochondrial dysfunction in ALS. *Prog. Neurobiol.* **97,** 54–66 (2012).

42. Knott, A. B., Perkins, G., Schwarzenbacher, R. & Bossy-Wetzel, E. Mitochondrial fragmentation in neurodegeneration. *Nat. Rev. Neurosci.* **9,** 505–18 (2008).

43. Kawamata, H. & Manfredi, G. Mitochondrial dysfunction and intracellular calcium dysregulation in ALS. *Mech. Ageing Dev.* **131,** 517–526 (2010).

44. Carrì, M. T., Valle, C., Bozzo, F. & Cozzolino, M. Oxidative stress and mitochondrial damage: importance in non-SOD1 ALS. *Front. Cell. Neurosci.* **9,** 41 (2015).

45. Von Lewinski, F. & Keller, B. U. Ca2+, mitochondria and selective motoneuron vulnerability: Implications for ALS. *Trends in Neurosciences* **28,** 494–500 (2005).

46. Mattson, M. R. Calcium and neurodegeneration. *Aging Cell* **6,** 337–350 (2007).

47. Mattson, M. P. Pathways towards and away from Alzheimer's disease. *Nature* **430,** 631–639 (2004).

48. Marambaud, P., Dreses-Werringloer, U. & Vingtdeux, V. Calcium signaling in neurodegeneration. *Mol. Neurodegener.* **4,** 20 (2009).

49. Bezprozvanny, I. B. Calcium signaling and neurodegeneration. *Acta Naturae* **2,** 72–82 (2010).

50. Bernard-Marissal, N. *et al.* Reduced Calreticulin Levels Link Endoplasmic Reticulum Stress and Fas-Triggered Cell Death in Motoneurons Vulnerable to ALS. *J. Neurosci.* **32,** 4901–4912 (2012).

51. Saxena, S. & Caroni, P. Selective Neuronal Vulnerability in Neurodegenerative Diseases: From Stressor Thresholds to Degeneration. *Neuron* **71,** 35–48 (2011).

52. Grosskreutz, J., Van Den Bosch, L. & Keller, B. U. Calcium dysregulation in amyotrophic lateral sclerosis. *Cell Calcium* **47,** 165–174 (2010).

53. Coussee, E. *et al.* G37R SOD1 mutant alters mitochondrial complex I activity, Ca2+ uptake and ATP production. *Cell Calcium* **49,** 217–225 (2011).

54. Tradewell, M. L., Cooper, L. A., Minotti, S. & Durham, H. D. Calcium dysregulation, mitochondrial pathology and protein aggregation in a culture model of amyotrophic lateral sclerosis: Mechanistic relationship and differential sensitivity to intervention. *Neurobiol. Dis.* **42,** 265–275 (2011).

55. Fuchs, A. *et al.* Selective mitochondrial Ca2+ uptake deficit in disease endstage vulnerable motoneurons of the SOD1G93A mouse model of amyotrophic lateral sclerosis. *J. Physiol.* **591,** 2723–45 (2013).

56. Saxena, S. *et al.* Neuroprotection through Excitability and mTOR Required in ALS Motoneurons to Delay Disease and Extend Survival. *Neuron* **80,** 80–96 (2013).

57. Camandola, S., Cutler, R. G., Gary, D. S., Milhavet, O. & Mattson, M. P. Suppression of calcium release from inositol 1,4,5-trisphosphate-sensitive stores mediates the anti-apoptotic function of nuclear factor-κB. *J. Biol. Chem.* **280,** 22287–22296 (2005).

58. Furukawa, K. & Mattson, M. P. The transcription factor NF-KB mediates increases in calcium currents and decreases in NMDA- and AMPA/kainate-induced currents induced by tumor necrosis factor-a in hippocampal neurons. *J. Neurochem.* **70,** 1876–1886 (1998).

59. Navarrete, M. & Araque, A. The Cajal school and the physiological role of astrocytes: a way of thinking. *Front. Neuroanat.* **8,** 33 (2014).

60. Yamanaka, K. *et al.* Astrocytes as determinants of disease progression in inherited amyotrophic lateral sclerosis. *Nat. Neurosci.* **11,** 251–3 (2008).

61. Barbeito, L. H. *et al.* A role for astrocytes in motor neuron loss in amyotrophic lateral sclerosis. *Brain Res. Brain Res. Rev.* **47,** 263–74 (2004).

62. Ferraiuolo, L. *et al.* Dysregulation of astrocyte-motoneuron cross-talk in mutant superoxide dismutase 1-related amyotrophic lateral sclerosis. *Brain* **134,** 2627–2641 (2011).

63. Rothstein, J. D. & Kuncl, R. W. Neuroprotective strategies in a model of chronic glutamate-mediated motor neuron toxicity. *J Neurochem* **65,** 643–651 (1995).

64. Yin, H. Z. & Weiss, J. H. Marked synergism between mutant SOD1 and glutamate transport inhibition in the induction of motor neuronal degeneration in spinal cord slice cultures. *Brain Res.* **1448,** 153–162 (2012).

65. Fritz, E. *et al.* Mutant SOD1-expressing astrocytes release toxic factors that trigger motoneuron death by inducing hyperexcitability. *J. Neurophysiol.* **109,** 2803–14 (2013).

66. Kawamata, H. *et al.* Abnormal Intracellular Calcium Signaling and SNARE-Dependent Exocytosis Contributes to SOD1G93A Astrocyte-Mediated Toxicity in Amyotrophic Lateral Sclerosis. *J. Neurosci.* **34,** 2331–2348 (2014).

67. Cassina, P. *et al.* Mitochondrial dysfunction in SOD1G93A-bearing astrocytes promotes motor neuron degeneration: prevention by mitochondrial-targeted antioxidants. *J. Neurosci.* **28,** 4115–22 (2008).

68. Martorana, F. *et al.* The BH4 domain of Bcl-X L rescues astrocyte degeneration in amyotrophic lateral sclerosis by modulating intracellular calcium signals. *Hum. Mol. Genet.* **21,** 826–840 (2012).

69. Shimomura, O., Johnson, F. H. & Saiga, Y. Extraction, Purification and Properties of Aequorin, a Bioluminescent Protein from the Luminous Hydromedusan,Aequorea. *J. Cell. Comp. Physiol.* **59,** 223–239 (1962).

70. Johnson, F. & Shimomura, O. Preperation and use of Aequorin for rapid microdetermination of calcium in biological systems. *Nat. new Biol.* **237,** 287–288 (1972).

71. de la Fuente, S., Fonteriz, R. I., de la Cruz, P. J., Montero, M. & Alvarez, J. Mitochondrial free [Ca(2+)] dynamics measured with a novel low-Ca(2+) affinity aequorin probe. *Biochem. J.* **445,** 371–6 (2012).

72. Bonora, M. *et al.* Subcellular calcium measurements in mammalian cells using jellyfish photoprotein aequorin-based probes. *Nat. Protoc.* **8,** 2105–18 (2013).

73. Lim, D., Bertoli, A., Sorgato, M. C. & Moccia, F. Generation and usage of aequorin lentiviral vectors for Ca2+ measurement in sub-cellular compartments of hard-to-transfect cells. *Cell Calcium* **59,** 228–239 (2016).

74. Greotti, E., Wong, A., Pozzan, T., Pendin, D. & Pizzo, P. Characterization of the ER-Targeted Low Affinity Ca2+ Probe D4ER. *Sensors* **16,** 1419 (2016).

75. Palmer, A. E. *et al.* Ca2+ Indicators Based on Computationally Redesigned Calmodulin-Peptide Pairs. *Chem. Biol.* **13,** 521–530 (2006).

Introductory Note

My PhD activity was focused on two major projects, both relating to the involvement of Ca^{2+} dysmetabolism in ALS pathogenesis. The first one was aimed at generating and validating novel adeno-associated viral vectors for the selective expression in motor neurons of gene-encoded Ca^{2+} probes targeted to different cell compartments, thereby allowing *in vitro* and *in vivo* measurements of local Ca^{2+} homeostasis in cells that are the primary target of ALS injury. The second project aimed at identifying local perturbations of Ca^{2+} homeostasis in primary spinal astrocytes, derived from a well-characterised genetic murine model of ALS, as a possible mechanism of pathogenesis.

The two parts of the thesis are presented in the format of scientific papers, such as they were presented for peer reviewing. The first part of the work is indeed ready to be submitted for revision to Scientific Reports, while the second part is a work in progress.

4. Generation and validation of novel adeno-associated viral vectors for the analysis of Ca^{2+} homeostasis in motor neurons

Rosa Pia Norante[1#], Maria Lina Massimino[2#], Paolo Lorenzon[1§], Agnese De Mario[1], Mattia Albiero[3], Maria Catia Sorgato[1,2], Raffaele Lopreiato[1], Alessandro Bertoli[1*]

[1]Department of Biomedical Science, University of Padova, Italy
[2]CNR Neuroscience Institute, Padova, Italy
[3]Department of Medicine, and Venetian Institute of Molecular Medicine, Padova, Italy

[#]These Authors contributed equally to this work
[§]Current address: Department of Integrative Medical Biology (IMB), Umeå Universitet, 901 87 Umeå, SE

[*]To whom correspondence should be addressed:
Alessandro Bertoli, Dept. of Biomedical Science, University of Padova
Via U. Bassi 58/B, 35131 Padova, Italy
Tel: +39 049 827 6150
Fax: +39 049 827 6363
E- mail: alessandro.bertoli@unipd.it

Key words: Ca^{2+}; calcium homeostasis; genetically-encoded Ca^{2+} indicators; cameleon; motor neuron; adeno-associated virus; mitochondria; endoplasmic reticulum; amyotrophic lateral sclerosis

4.1 Abstract

A finely tuned Ca^{2+} homeostasis in restricted cell domains is of fundamental importance for neurons, in which transient Ca^{2+} oscillations direct the proper coordination of electro-chemical signals and overall neuronal metabolism. Once such a precise regulation is unbalanced, however, neuronal functions and viability are severely compromised. Accordingly, disturbed Ca^{2+} metabolism has often been claimed as a major contributor to different neurodegenerative disorders, such as amyotrophic lateral sclerosis that is characterised by the selective damage of motor neurons (MNs). This notion highlights the need for probes allowing the specific and precise analysis of local Ca^{2+} dynamics in MNs. In this work, we generated and functionally validated adeno-associated viral vectors for the expression of genetically-encoded fluorescent Ca^{2+} indicators targeted to different cell domains under the transcriptional control of a MN-specific promoter. We demonstrated that the probes are specifically expressed, and allow reliable local Ca^{2+} measurements, in MNs from murine primary spinal cord cultures, and can also be expressed *in vivo* in spinal cord MNs upon systemic administration to newborn mice. Preliminary analyses have shown larger Ca^{2+} responses following stimulation of AMPA-sensitive ionotropic glutamate receptors in the cytosol of MNs from a murine genetic model of ALS compared to the healthy counterpart.

4.2 Introduction

Ca^{2+} ions play a fundamental role in all cell types by controlling an impressive number of signalling events. Therefore, a precise control of Ca^{2+} homeostasis in the cytosol and other cell compartments/organelles – performed by several systems like pumps, channels, transporters and Ca^{2+}-buffering proteins – is essential for cell physiology. In neurons, local Ca^{2+} fluctuations have a key physiologic impact, by controlling the spatiotemporal pattern of electrochemical signals, neurite outgrowth, synaptic plasticity and the patterning of dendritic spines (major factors in the neurochemical/neuroanatomical establishment of learning and memory), and, last but not the least, cell survival. Not surprisingly, small changes in Ca^{2+} dynamics can lead to pathological conditions[1], and derangements of Ca^{2+} homeostasis has been frequently indicated as a major contributor to the onset of various neurodegenerative disorders, such as Alzheimer's, Parkinson's, and Huntington's disease[2].

Among neurons, MNs are particularly sensitive to noxious cell Ca^{2+} overloads because they possess low levels of Ca^{2+}-buffering proteins[3,4]. Also, they express high levels of Ca^{2+}-permeable α-amino-5-methyl-3- hydroxisoxazolone-4-propionate (AMPA) receptors that lack the GluR2 subunit, which makes them more vulnerable to dysregulation of intracellular Ca^{2+} homeostasis and excitotoxicity[5]. Not surprisingly, perturbed Ca^{2+} homeostasis has been claimed as a major actor in the pathogenesis of different MN disorders, such as amyotrophic lateral sclerosis (ALS) [6,7]and spinal muscular atrophy [8]. The above notions highlight the need for molecular tools, such as suitable Ca^{2+} indicators, for the specific and precise analysis of Ca^{2+} movements in different sub-cellular compartments of MNs.

Historically, cell Ca^{2+} imaging has been developed in two different ways: the improvement of Ca^{2+} indicators and, in parallel, the progress of appropriate and sophisticated instrumentations (like confocal or multi-photon microscopy) to reach the capability of studying Ca^{2+}mobility *in vitro* and *in vivo*. There are two major classes of Ca^{2+} indicators: chemical probes and genetically encoded calcium indicators (GECI). The first ones are hybridizations of small Ca^{2+}-chelating molecules and a fluorophore. This class of probes include fura-2, quin-2, indo-1 and fluo-3, which are the first kind of indicators used for Ca^{2+} measurements in cells[9]. A second class of probes is that of GECI, which includes different types of engineered proteins such as green fluorescent protein (GFP)-derived fluorescent probes (e.g., GCamp), bioluminescent probes (e.g., aequorin) and fluorescence (or Förster) resonance energy transfer (FRET)-based indicators (e.g., cameleons). A clear advantage of these probes is that – at difference from chemical indicators – they can be genetically targeted to different cell domains/compartments for local Ca^{2+} measurements. On the other hand, they suffer

from the difficulty to be efficiently expressed in cells, in particular in primary neurons, which can be now easily overcome by use of viral expression vectors[10–12].

Cameleon probes are based on FRET, a well-known quantum mechanical process consisting in the energy transfer from an exited fluorescent donor to an acceptor fluorophore placed in close proximity. Therefore, when FRET occurs, an increased fluorescence of the acceptor, together with a decreased fluorescence of the donor can be observed and quantified. In last years, several studies based on site-directed mutagenesis have led to the generation of improved cameleon Ca^{2+} probes, by increasing the brightness of the FRET acceptor in response to Ca^{2+} fluctuations, reducing the possible competitive effect of endogenous CaM, and extending the affinity of cameleons for Ca^{2+} to render the probes suitable for Ca^{2+} measurements in different cell districts. In particular, different kinds of cameleon exist (classified as D1, D2, D3 and D4[13]) covering a wide K_d range for Ca^{2+} that allow scientists to choose the best probe for the specific cell compartment under study[13–15].

In this work, we have generated and functionally validated adeno-associated viral (AAV)-based vectors for the expression of cameleons targeted to different cell domains (i.e., cytosol, mitochondrial matrix, or endoplasmic reticulum (ER) lumen) under the transcriptional control of a MN-specific promoter. We demonstrate that such probes are specifically expressed in MNs (and not in other cell types) in primary cell cultures from the mouse spinal cord, and that they allow reliable Ca^{2+} measurements in the target cell compartment. Pilot experiments also demonstrate altered Ca^{2+} homeostasis in the cytosol of primary MNs from a genetic model of ALS, and that the generated AAV expression vectors can be suited for the *in vivo* expression of cameleons in spinal cord MNs in mice.

4.3 Results

Given the plausible implication of perturbed Ca^{2+} homeostasis in the pathogenesis of MN [6–8] in this study we sought to generate and validate expression systems for GECI that were suited for the assessment of local Ca^{2+} fluctuations in MNs. To this purpose, we have engineered adeno-associated virus (AAV) plasmids (pAAV) for the expression of cameleon probes targeted to the cytosol (pAAV-[Hb9_AB]-D1cpv), the mitochondrial matrix (pAAV-[Hb9_AB]-4mtD3cpv) and the ER lumen (pAAV-[Hb9_AB]-D4ER), under the control of a motor neuron-specific, homeobox Hb9-derived, promoter (Fig. S1, Supplementary online material).

To validate such vectors for the specific recording of Ca^{2+} fluxes in MNs, we firstly checked the expression of our AAV-driven probes in the immortalised NSC-34 cell line that – when properly differentiated – displays several typical properties of motor neurons[16,17] including the transcriptional activation of the Hb9 gene[18]. We therefore checked the expression of the three cameleon probes in NSC-34 cells, transduced with the AAV vectors, either cultured under proliferating conditions or induced to differentiate by treatment with retinoic acid (7 days, Fig. S2, Supplementary online material). We observed that all cameleons were abundantly expressed in differentiated cells but not in cells under active proliferation, suggesting that the Ca^{2+} probes were specifically expressed in cells resembling a MN phenotype (Fig 1).

We then analysed by confocal microscopy the expression of cameleons in primary cultures from the spinal cord of mice expressing human superoxide dismutase 1 (hSOD1), either wild-type (WT) or bearing the ALS-related mutation (G93A). After 12 days of growth, such cultures contain different cell types, including mature MNs resembling their counterparts in intact spinal cord, both morphologically and for the expression of specific biological markers, such as the neurofilament protein SMI32. As described in Fig. 2, showing cultures from hSOD1(WT) mice, after transduction of such cell cultures with the AAV vectors, the cameleons (green signal, panels A,E,I) were expressed only in SMI32-positive cells (red signal, panels B,F,J) but not in other cell types (highlighted by nuclear staining, blue signal, panels C,G,K), providing evidence that the Hb9 promoter-driven expression of the Ca^{2+} probes is specific for MNs (merge, panels D,H,L).

The above conclusion is further reinforced by the finding that the AAV vectors are unable to drive the expression of the mitochondria-targeted cameleon in (almost pure) primary cultures of cortical (Fig. S3, Supplementary online material, panels A,B), hippocampal (panels C,D) or cerebellar granule (panels E,F) neurons, or spinal astrocytes (panels G,H).

Next we checked that the cameleon had the expected sub-cellular[14,19,20] distribution in primary MNs. As shown in Fig. 3, each probe (green signal, panels A,D,G) co-localised (yellow signal,

merged images of panels C,F,I) with immuno-labelled markers of the corresponding target compartment, i.e., HSP90 for the cytosol (panel B), Tom20 for mitochondria (panel E), and calreticulin for the ER lumen (panel H), indicating that the probes are correctly processed and delivered to the target site in AAV transduced MNs.

ALS is a fatal neurodegenerative disorder that occurs on sporadic or genetic grounds, leading to a selective and progressive loss of MNs in the spinal cord, brainstem and cerebral cortex, thereby resulting in severe motor deficits and – eventually – to death [21,22]. Since perturbations of Ca^{2+} homeostasis in MNs have been often claimed as a crucial event in disease progression[7,23] we tested the applicability of the novel Ca^{2+}-probe encoding vectors to the comparative analysis of local Ca^{2+} homeostasis in MNs from the hSOD1(G93A) ALS mouse model and the healthy hSOD1(WT) counterpart (the hSOD1 expression level being the same for both the genotypes). The cameleon probes of choice have great ratiometric sensitivity and large dynamic range, thereby allowing to detect small changes in Ca^{2+} concentration over the noise in the target compartment [13]. In this work we did not calculated absolute Ca^{2+} concentrations that could be determined by suitable calibration procedures[13], but simply reported the ratio between the acceptor and the donor fluorescence of the FRET-based probes, which – however – is sufficient for comparative analyses. Nonetheless, such experiments demonstrated that all cameleon probes were functional, and indicated that hSOD1(G93A)-expressing MNs have larger cytosolic Ca^{2+} transients following AMPA stimulation, compared to SOD1(WT) MNs (Fig 4A,B). Conversely, no significant difference was observed in AMPA-stimulated Ca^{2+} fluxes in the mitochondrial matrix (Fig. 4C,D). Also the ER-targeted cameleon was properly functioning, allowing the measurement of ER Ca^{2+} discharge upon stimulation with caffeine. Also in this case, no difference was observed between MNs with the two genotypes (Fig. 4E,F).

Finally, we probed the use of the developed AAV-based expression systems for *in vivo* experiments. To this purpose, we injected the AAV vector coding for the mitochondrial or the ER cameleon into the superficial temporal vein of newborn hSOD1(WT) mice, and evaluated the expression efficiency of the probes in spinal cord sections 4 weeks later. By use of a fluorescence stereo-microscope, we observed an intense and diffuse signal in tissue samples of mice transduced with either the mitochondrial (Fig. 5A-C) or the ER (Fig. 5D-F) cameleon. Images collected at a higher magnification by a fluorescence microscope (Fig. 5G-I) showed that cells transduced with the ER probe had MN morphology, confirming the cell specificity of the expression system also in *in vivo* paradigms.

4.4 Discussion

Recombinant AAVs are a powerful means for *in vivo* gene delivery[24,25] and for the transduction of primary cell cultures that are particularly hard to transfect, such as neurons[26,27]. AAVs display low cytotoxicity and immunogenicity, are safe for the operator, and are suitable for long term gene expression in non-dividing cells with relatively high gene delivery efficiency, depending on the cell type[28].

In this work, we have generated pAAV plasmids encoding cameleon Ca^{2+} probes, genetically targeted to different cell compartments, under the transcriptional control of a MN-specific promoter. Given that AAV vectors has limited cloning capacity (i.e., large plasmids can hardly be packaged into AAV viral particles), we have chosen a genetically engineered minimal promoter of the Hb9 gene (Hb9_AB), which is only about 550 bp in length and has already been demonstrated to specifically drive the expression of a transgene into MNs, both *in vitro* and *in vivo*[29]. For the preparation of the viral particles, we have chosen the AAV9 serotype because of its broad tropism, including the capacity to target neurons[28]. We have demonstrated that the engineered AAV vectors are suitable for the specific expression of the cameleons targeted to the cytosol, the mitochondrial matrix and the ER lumen of MNs from spinal cord primary cultures of mice, and allows measuring Ca^{2+} responses to proper stimuli in such cellular districts. These vectors have several advantages with respect to other expression systems or the use of ubiquitous promoters. Indeed, they allow Ca^{2+} measurements in single primary MNs with no need for difficult and time-consuming MN purification steps. In addition, MN Ca^{2+} measurements can be performed in a more physiologic environment, containing glial cells and other neuronal types, compared to pure MN cultures.

We did not estimate the rate of AAV-mediated infection of MNs. However, a substantial number of SMI32-positive cells contained the Ca^{2+} probes at an expression level that easily allowed single cell recordings of Ca^{2+} dynamics. The transduction efficiency under our experimental setting was much higher than that achieved by transfection with plasmidic vectors, with which cameleon-expressing MNs were rarely found in each preparation, also when using a constitutive and ubiquitous (cytomegalovirus) or the pan-neuronal human synapsin1 (hSyn) promoter (data not shown).

Among GECI, the ratiometric cameleon probes have several advantages, including low risk of artifacts, high sensitivity, good dynamic range, and the possibility to provide absolute Ca^{2+} concentration values upon proper calibration procedures[13]. In addition, engineering of mutant cameleons have provided researcher with several cameleons displaying a wide range of K_ds for

Ca^{2+}, thereby allowing reliable measurements of basal Ca^{2+} levels and evoked Ca^{2+} movements depending on the target cell compartment, the cell type and the desired stimulation protocol[14,19].

For cytosolic Ca^{2+} measurements we have cloned into pAAV vectors the D1-based probe[30], which, although it is probably not the best suited cameleon for reliable basal Ca^{2+} measurements, allowed us to measure cytosolic fluctuations of the ion in MNs following AMPA stimulation.

Correct Ca^{2+} handling by mitochondria is essential for cell physiology. On the one hand, the fine regulation of mitochondrial Ca^{2+} levels controls the mitochondrial production of ATP, because different mitochondrial enzymes rely on local Ca^{2+} concentration for their activity. On the other hand, mitochondria are a major Ca^{2+}-buffering system avoiding noxious cytosolic Ca^{2+} overloads. While it is assumed that resting mitochondrial Ca^{2+} concentration is in the order of 10^{-1} μM, upon stimulation promoting Ca^{2+} entry from the extracellular space or its release from the ER, Ca^{2+} levels in the mitochondrial matrix may reach up to 10^{2} μM, depending on the cell type and the stimulus[31]. Therefore, we have selected the 4mtD3cpv cameleon that, for its K_d and dynamic range, has been proved useful for measuring mitochondrial Ca^{2+} dynamics[13]**.**

Finally, for the measurements of Ca^{2+} homeostasis in the ER lumen, we have chosen the recently generated D4ER probe[14] that have been proved useful for comparative Ca^{2+} measurements in an experimental setting of neurodegenerative disorders[32].

Notably, cameleons are mostly expressed in SMI32-positive α-MNs, enriched in the anterior ventral horn of the spinal cord[33,34],which are particularly vulnerable to (AMPA-mediated) excitotoxic challenge and ALS-related damage[6,7]. Thus, to prove the efficacy of the probes to monitor local Ca^{2+} fluctuations in MNs, we have compared the response of MNs from mice expressing the ALS-related hSOD1(G93A) mutant, or the hSOD(WT)-expressing counterpart, to selected stimuli. In particular, we investigated Ca^{2+} responses in the cytosol and mitochondria to AMPA stimulation because excitoxicity has been proposed to contribute crucially to MN injury in ALS, probably as a consequence of glutamate-triggered Ca^{2+} overload[7,35]. Both the cytosolic and mitochondrial probe allowed the assessment of AMPA-mediated cell Ca^{2+} response, and underscored a larger entry of the ion in the cytosol, but not in mitochondria, of ALS MNs compared to the healthy controls, thus supporting the idea that Ca^{2+} overload may be involved in ALS MN damage. Also the ER cameleon was properly functioning, and monitored the ER Ca^{2+} discharge promoted by caffeine[36,37], with no difference being observed between the two SOD1 genotypes.

To our knowledge, the novel vectors we generated in this work allowed for the first time to directly monitoring local Ca^{2+} fluctuations in subcellular compartments of primary mouse MNs, thereby

providing valuable and versatile tools for expanding our knowledge on Ca^{2+}-related pathogenic routes in ALS and other neuromuscular diseases. With this respect, it is worth underlining that other GECI-encoding sequences can be easily cloned into the generated MN promoter-containing pAAV scaffold, thereby providing expression systems for Ca^{2+} probes with different properties (e.g., K_d) for appropriate Ca^{2+} measurements under different experimental protocols.

Importantly, we provided evidence that the AAV vectors can also drive the *in vivo* expression of the Ca^{2+} probes. This result was achieved by systemic administration of the virus, which is by far less invasive and arduous than local injection in the spinal cord of live mice.

4.5 Materials and Methods

4.5.1 Plasmid construction

Multiple pAAV have been generated, for the expression of the FRET-based cameleon Ca^{2+} probes targeted to different cellular compartment (i.e. cytosol, mitochondrial matrix and ER lumen[13,14,19,20] under the control of either a minimal promoter (Hb9_AB) derived from the (MN)-specific promoter of the Hb9 gene[29], or the pan-neuronal hSyn promoter.

Starting from the pAAV-[hSyn]-ChR2/EYFP vector (Addgene, cat. # 26973) (Fig. S1, panel A), we inserted the sequence coding for the cytosolic probe (D1cpv), previously isolated by BamHI-EcoRI cleavage of a pcDNA3-D1cpv plasmid (kindly provided by Dr. Roger Tsien, University of California, San Diego, USA;[13,19]), at BamHI-EcoRI sites. After digestion, purified DNA fragments were ligated in vitro by T4 DNA ligase, and *E. coli* TOP10 cells were transformed to recover the pAAV-[hSyn]-D1cpv plasmid (Fig. S1, panel B). Similarly, at KpnI-HindIII sites of the pAAV-[hSyn]-ChR2/EYFP vector we inserted the sequence coding for the ER lumen probe (D4ER), which was previously amplified by PCR using as template the pcDNA3- D4ER plasmid (kindly provided by Dr. Paola Pizzo, Dept. of Biomedical Science, Univ. of Padova) and the primers ER-K1-F and ER-H3-R (sequences reported in the Supplementary online material). The PCR product was digested with KpnI-HindIII, and purified DNA fragments ligated as indicated above, generating the pAAV-[hSyn]-D4ER plasmid (Fig. S1, panel B).

Finally, we performed the substitution of the [hSyn] promoter sequence with the ~550 bp motor neuron specific promoter [Hb9_AB], which was previously amplified by PCR using as template the Bg.Hb9_AB plasmid[29] (kindly provided by Dr. Caterina Bendotti, IRCCS Istituto di Ricerche Farmacologiche Mario Negri, Milano, Italy), and primers AB-M1-F and AB-K1-R (sequences reported in the Supplementary online material). The PCR product, subjected to MluI-KpnI cleavage and purified, was then ligated to both pAAV-[hSyn]-D1cpv and pAAV-[hSyn]-D4ERcpv plasmidic fragments digested with the same enzymes that removed the hSyn promoter sequence. We also generated the pAAV-[Hb9_AB]-4mtD3cpv vector, expressing the probe targeted to the mitochondrial matrix (4mtD3cpv), by replacing the hSyn promoter of the pAAV-[hSyn]-4mtD3cpv plasmid (a generous gift by Dr. Paola Pizzo, Dept. of Biomedical Science, Univ. of Padova), with the Hb9_AB promoter. After transformation and selection of *E. coli* cells, some positive clones were isolated, recombinant plasmids were checked by specific DNA restriction, and finally validated by sequencing. All enzymes were from New England Biolabs, excepted the high-fidelity DNA polymerase (KAPA Biosystems), and DNA primers (Life Technologies). DNA manipulations have been performed accordingly to standard methods[38] and to manufacturer's instructions.

Detailed maps and plasmids sequences are all available upon request to the corresponding author.

AAV viral particles (AAV9 serotype) were commercially produced by Vigene Biosciences with viral titer ranging from 2×10^{13} to 10×10^{13} GC/ml.

4.5.2 Animals

Tg mice expressing WT hSOD1 or the ALS-related G93A mutant of hSOD1 (B6SJL(Tg-SOD1)2Gur/J and B6SJL(Tg-SOD1*G93A)1Gur/J mice, respectively) were purchased from The Jackson Laboratories. Since the transgenes contains the entire hSOD1 gene, including the endogenous SOD1 promoter[39], the expression of both WT and mutant hSOD1 mimics the natural pattern of SOD1 expression. The colonies were maintained by breeding hemizygous (Tg) males to wild-type B6SJLF1/J hybrid females. Embryos and newborns were genotyped (as described in supplementary materials), and used for subsequent experiments. All aspects of animal care and experimentation were performed in compliance with European and Italian (D.L. 26/2014) laws concerning the care and use of laboratory animals. The authors' Institution has been accredited for the use of experimental mice by the Italian Ministry of Health, and by the ethical committee of the University of Padova (Organismo Preposto al Benessere degli Animali, OPBA).

For mouse genotyping and NSC34 cell culturing, see Supplementary Online Material.

4.5.3 Primary cultures

Primary spinal cord cell cultures (containing MNs and other cell types) were established from E12.5 mouse embryos according to Henderson's protocol (Mettling *et al.* 1995)[40]. Briefly, spinal cords were dissected from individual embryos in Hybernate medium (Gibco) added with 2% (v/v) B27 supplement (Gibco), and tissue was cut (< 1 mm pieces) and incubated (8 min, 37 °C) in a buffer containing NaCl (124 mM), KCl (5.4 mM), NaH_2PO_4 (1 mM), glucose (3.6 mM), HEPES (25 mM, pH 7.4), added with BSA [0.3% (w/v)] and trypsin [0.025% (w/v)].

Then, cells were gently dissociated in a buffer made of Leibovitz's medium (L15, Gibco) supplemented with sodium bicarbonate [7.5% (w/v)], horse serum [HS, 2% (v/v)], glucose [7.2% (w/v)], progesterone [0.1% (w/v)], insulin [1% (w/v)] , putrescine [1% (w/v)], conalbumin [1% (w/v)], sodium selenite [0.1% (w/v)] , BSA [0.4% (w/v)] and DNase I [0.1 mg/ml].

The cell suspension was then centrifuged (500 x g, 5 min, RT) over a cushion of BSA [4% (w/v)] (in the above medium), after which cells were recovered from the bottom of the tube, resuspended in a MN culture medium consisting of Neurobasal medium (Gibco) supplemented with HS [2% (v/v)], B27 [2% (v/v)], L-glutamine [0.05 mM], glutamate [25 µM], mercaptoethanol [25 µM], BDNF [10 ng/ml], GDNF [10 ng/ml], and CNTF [10 ng/ml], penicillin [100 U/ml], streptomycin

[100 μg/ml]. Cells were then plated at a density of approximately 500.000 cells/well in 12-wells culture plates containing (18 mm diameter) glass coverslips coated with poly-D-ornithine (1.5 μg/ml in sterilized bidistilled H_2O, 2 h, RT) and then with laminin (3 μg/ml in L15 medium, 3 h, 37 °C in a 5% CO_2 atmosphere), and grown (37 °C in a 5% CO_2 atmosphere).

Primary cultures of CGN and cortical neurons were prepared as described in De Mario *et al.* (2015)[41]. Hippocampal neurons were prepared following the same procedures for cortical neurons, except that they were grown in Neurobasal medium added with FBS [10% (v/v)].

Primary cultures of spinal astrocytes were isolated from newborn mice and cultured as described previously in Martorana *et al*. (2012)[42]. Once the cultures reached the confluence, they were re-plated at the optimal density 80.000 cells/well in 24-well plates containing glass coverslips and maintained in minimal essential medium (MEM, Gibco), supplemented with FBS [10% (v/v)], L-glutamine [2 mM], glucose in phosphate buffered saline [PBS, 0.3% (w/v)], penicillin [100 U/ml], streptomycin [100 μg/ml].

On day 2 from plating, all primary cultures were transduced with the AAV9-Hb9-cyt or AAV9-Hb9-mt or AAV9-Hb9-ER (0.5 μl of viral suspension containing 3×10^{10} GC/ml) and used in experiments at different times depending on the cell type.

4.5.4 Immunocytochemistry

For immunocytochemical analysis, cells were firstly washed in ice-cold PBS, and fixed (20 min, RT) in paraformaldehyde [PFA, 4% (w/v)] in PBS. After washing in PBS, cells were permeabilized in PBS containing Triton X-100 [1 h, RT, 0.02% (w/v)] and then incubated (overnight, 4 °C) with the following primary antibodies [Ab diluted in 1% (w/v) BSA, in PBS]: anti-SMI32 mouse monoclonal (m) Ab (1:200, Covance, cat. n. SMI-32R & SMI-32P); anti-glial fibrillary acidic protein (GFAP) rabbit polyclonal (p) Ab (1:500, Dako, cat. n. Z0334); anti-microtubule-associated protein-2 (MAP-2) chicken pAb (1:1000, Abcam, cat. n. ab5392); anti-calreticulin rabbit pAb (1:50, Stressgen, cat. n. ADI-SPA-600-J); anti-Hsp90 mouse mAb (1:100, BioScience, cat. n. 610418BD); anti-Tom20 rabbit pAb (1:50, Santa Cruz Biotechnologies, cat. n. sc-11415). After extensive washings in PBS, cells were incubated (1 h, 37 °C) with the following secondary antibodies, depending on the used primary Ab: Alexa Fluor 555-conjugated anti-mouse IgG (1:500, Molecular Probes); rhodamine-conjugated anti-rabbit IgG (1:100, Dako); Alexa Fluor 568-conjugated anti-chicken IgG (1:500, Molecular Probes). Cell nuclei were counter-stained with Hoechst 33342 (5 μg/ml, Sigma), and coverslips were finally washed in PBS, mounted in montage solution [8% Mowiol 40-88 (Sigma) in glycerol and PBS (1:3 (v/v)], and observed with an inverted fluorescence microscope (Leica CTR6000) equipped with a computer-assisted charge-coupled camera (Orca

Flash 4.0, Hamamatsu), or with a confocal microscope system (Leica TCS-SP5), which also allowed the acquisition and analysis of digital images.

4.5.5 Ca^{2+} imaging

For Ca^{2+} imaging, 12 days after plating, cells were mounted into an open-topped chamber and maintained under perfusion with a modified Krebs-ringer buffer (NaCl 125 mM, KCl 5 mM, KH_2PO_4 0.4 mM, $MgSO_4$ 1 mM, glucose 5.5 mM, HEPES 20 mM, pH 7.4) containing $CaCl_2$ (2 mM) (KRB), through a temperature-controlled (37 °C) instrument (TC-324B, Warner Instruments,). Cells were stimulated with AMPA (Tocris, 25 μM) for cytosolic and mitochondrial Ca^{2+} measurements, or with 100 μM caffeine for ER Ca^{2+} measurements (both stimuli carried out in KRB).

Cell were analysed using a DM6000 inverted microscope (Leica) with a 40X oil objective (HCX Plan Apo, NA 1.25). Excitation light produced by a 410nm led (LZ1-00UA00-LED, Led Engin) was filtered at the appropriate wavelength (425 nm) through a band-pass filter, and the emitted light was collected through a dichroic mirror (515 DCXR, Chroma Technologie), and a beam-splitter (OES) with emission filters (Chroma Technologies) HQ 480/40M (for CFP) and HQ 535/30M (for YFP). The beam-splitter permits the collection of the two emitted wavelengths at the same time, thus preventing any artefact due to uncontrolled movement of the recording chamber and/or intracellular organelles. Images were acquired using an IM 1.4C cooled CCD (Jenoptik Optical Systems) attached to a 12-bit frame grabber. Synchronization of the excitation source and the CCD was performed through a control unit ran by a custom-made software package (developed by C. Ciubotaru, Venetian Institute of Molecular Medicine, Padova, Italy), which was also used for image acquisition, with an exposure time of 100 ms and a time-shift of 0.5 s. The software allows with-time recordings of the ratio between the acceptor and the donor fluorescence intensity (R) (sampling rate = 1 s^{-1}) that is taken as a relative measurement of Ca^{2+} concentration.

4.5.6 *In vivo* AAV-mediated delivery of cameleons

For *in vivo* delivery of AAV vectors, we have used P1 hSOD1 WT mice, in light of previous reports demonstrating much higher transduction rates in newborns than in adult mice[43,44]. After anaesthesia by topical administration of lidocaine, neonatal hSOD1(WT)-expressing mice (P1) received 50 μl of viral suspension containing 3×10^{11} GC/ml of AAV9-Hb9-mt, AAV9-Hb9-ER, or vehicle (PBS), into the temporal vein using a Hamilton syringe with a 32-gauge needle. The injections were performed in laboratory Biosafety Level 2 (BL2).

Four weeks after the injection, animals were anesthetized by CO_2 before killing by cervical dislocation, and spinal cords were collected and successively fixed in PFA [24 h, 4°C, 4% (w/v)]. Post-fixed tissues were transferred to sucrose [30% (w/v)] in PBS (overnight, 4°C) for cryoprotection. 20 μm-thick sections were serially cut on a cryostat (Leica Microsystems), nuclei were counter-stained with Hoechst 33342 (see immunocytochemistry), mounted in montage solution on a glass coverslip, and observed with a fluorescence stereo-microscope (Leica M205-FA), or with an inverted fluorescence microscope (Leica CTR6000) equipped with a computer-assisted charge-coupled camera (Orca Flash 4.0, Hamamatsu).

4.5.7 Statistical analysis

Off-line analysis of FRET data was performed with the ImageJ software. YFP and CFP images were subtracted for the respective background signals, and distinctly analysed after choosing proper regions of interest (ROI) on selected cells. Subsequently, the ratio between YFP and CFP emission fluorescence intensity (F) was calculated ($R = F_{535}/F_{480}$) and reported as %. All the data are representative of at least n (indicated in the figures and/or figure legends) independent experiments, and are reported as mean ± standard error of the mean (SEM). Statistics were performed by unpaired Student's t test, with a p value < 0.05 being considered statistically significant.

Acknowledgements

The Authors are grateful to Caterina Bendotti (Istituto di Ricerche Farmacologiche M. Negri, Milano, Italy) and Marco Peviani (Univ. of Pavia, Italy) for the plasmid containing the Hb9_AB promoter; Roger Tsien (University of California, San Diego, USA) and Paola Pizzo (Univ. of Padova) for plasmids containing the cameleons. The Authors also thank Diana Pendin (Univ. of Padova) for help with Ca^{2+} measurements, and Marta Giacomello (Univ. of Padova) for helpful discussion on the experiments. This work was supported by grants from AriSLA Foundation (project LoCaLS 2013, to A.B.) and the University of Padova (PRAT CPDA121988/12 to M.C.S., and PRAT CPDA158035/15 to A.B.).

Author contributions

R.P.N., M.L.M., P.L., M.C.S., R.L. and A.B. conceived and designed the experiments; R.P.N., M.L.M., PL, A.D.M., M.A. and R.L. performed the experiments; R.P.N., M.L.M., and A.B. analysed data and wrote the manuscript.

Additional Information

Competing Financial Interests

The Authors declare no competing financial interest.

4.6 References

1. Rizzuto, R. & Pozzan, T. When calcium goes wrong: genetic alterations of a ubiquitous signaling route. *Nat. Genet.* **34,** 135–41 (2003).
2. Mattson, M. R. Calcium and neurodegeneration. *Aging Cell* **6,** 337–350 (2007).
3. Ince, P. *et al.* Parvalbumin and calbindin D-28k in the human motor system and in motor neuron disease. *Neuropathol. Appl. Neurobiol.* **19,** 291–299 (1993).
4. Bernard-Marissal, N. *et al.* Reduced Calreticulin Levels Link Endoplasmic Reticulum Stress and Fas-Triggered Cell Death in Motoneurons Vulnerable to ALS. *J. Neurosci.* **32,** 4901–4912 (2012).
5. Williams, T. L., Day, N. C., Ince, P. G., Kamboj, R. K. & Shaw, P. J. Calcium-permeable a-amino-3-hydroxy-5-methyl-4-isoxazole propionic acid receptors: A molecular determinant of selective vulnerability in amyotrophic lateral sclerosis. *Ann. Neurol.* **42,** 200–207 (1997).
6. Van Den Bosch, L., Van Damme, P., Bogaert, E. & Robberecht, W. The role of excitotoxicity in the pathogenesis of amyotrophic lateral sclerosis. *Biochim. Biophys. Acta - Mol. Basis Dis.* **1762,** 1068–1082 (2006).
7. Grosskreutz, J., Van Den Bosch, L. & Keller, B. U. Calcium dysregulation in amyotrophic lateral sclerosis. *Cell Calcium* **47,** 165–174 (2010).
8. Ruiz, R., Casañas, J. J., Torres-Benito, L., Cano, R. & Tabares, L. Altered intracellular Ca2+ homeostasis in nerve terminals of severe spinal muscular atrophy mice. *J. Neurosci.* **30,** 849–57 (2010).
9. Tsien, R. Y., Pozzan, T. & Rink, T. J. Calcium Homeostasis in Intact Lymphocytes : Cytoplasmic Free Calcium Monitored With a New , Intracellularly Trapped Fluorescent Indicator. 325–334
10. Lim, D., Bertoli, A., Sorgato, M. C. & Moccia, F. Generation and usage of aequorin lentiviral vectors for Ca2+ measurement in sub-cellular compartments of hard-to-transfect cells. *Cell Calcium* **59,** 228–239 (2016).
11. Peel, A. L. & Klein, R. L. Adeno-associated virus vectors: Activity and applications in the CNS. *J. Neurosci. Methods* **98,** 95–104 (2000).
12. Du, B., Wu, P., Boldt-Houle, D. M. & Terwilliger, E. F. Efficient transduction of human neurons with an adeno-associated virus vector. *Gene Ther.* **3,** 254–261 (1996).

13. Palmer, A. E. & Tsien, R. Y. Measuring calcium signaling using genetically targetable fluorescent indicators. *Nat. Protoc.* **1,** 1057–1065 (2006).

14. Greotti, E., Wong, A., Pozzan, T., Pendin, D. & Pizzo, P. Characterization of the ER-Targeted Low Affinity Ca2+ Probe D4ER. *Sensors* **16,** 1419 (2016).

15. Suzuki, J., Kanemaru, K. & Iino, M. Genetically Encoded Fluorescent Indicators for Organellar Calcium Imaging. *Biophysical Journal* (2015).

16. Cashman, N. R. *et al.* Neuroblastoma x Spinal Cord (NSC) Hybrid Cell Lines Resemble Developing Motor Neurons. *Dev. Dyn.* **221,** 209–221 (1992).

17. Eggett, C. J. *et al.* Development and characterisation of a glutamate-sensitive motor neurone cell line. *J. Neurochem.* **74,** 1895–1902 (2000).

18. Pinto, C., Cárdenas, P., Osses, N. & Henríquez, J. P. Characterization of Wnt/β-catenin and BMP/Smad signaling pathways in an in vitro model of amyotrophic lateral sclerosis. *Front. Cell. Neurosci.* **7,** 239 (2013).

19. Palmer, A. E. *et al.* Ca2+ Indicators Based on Computationally Redesigned Calmodulin-Peptide Pairs. *Chem. Biol.* **13,** 521–530 (2006).

20. Zampese, E. & Pizzo, P. Intracellular organelles in the saga of Ca 2+ homeostasis: Different molecules for different purposes? *Cell. Mol. Life Sci.* **69,** 1077–1104 (2012).

21. Cleveland, D. W. & Rothstein, J. D. From Charcot to Lou Gehrig: deciphering selective motor neuron death in ALS. *Nat. Rev. Neurosci.* **2,** 806–819 (2001).

22. Rowland, L. & Shneider, N. Amyotrophic Lateral Sclerosis. *N. Engl. J. Med.* **344,** 1688–1700 (2001).

23. Von Lewinski, F. & Keller, B. U. Ca2+, mitochondria and selective motoneuron vulnerability: Implications for ALS. *Trends in Neurosciences* **28,** 494–500 (2005).

24. Kollarik, M. *et al.* Transgene expression and effective gene silencing in vagal afferent neurons in vivo using recombinant adeno-associated virus vectors. *J. Physiol.* **588,** 4303–4315 (2010).

25. Fagoe, N. D., Eggers, R., Verhaagen, J. & Mason, M. R. J. A compact dual promoter adeno-associated viral vector for efficient delivery of two genes to dorsal root ganglion neurons. *Gene Ther.* **21,** 242–252 (2014).

26. Xu, Y. *et al.* Adeno-associated viral transfer of opioid receptor gene to primary sensory

neurons: a strategy to increase opioid antinociception. *Proc Natl Acad Sci U S A* **100,** 6204–6209 (2003).

27. Jin, L. *et al.* High-efficiency transduction and specific expression of ChR2opt for optogenetic manipulation of primary cortical neurons mediated by recombinant adeno-associated viruses. *J. Biotechnol.* **233,** 171–180 (2016).

28. Howard, D. B., Powers, K., Wang, Y. & Harvey, B. K. Tropism and toxicity of adeno-associated viral vector serotypes 1, 2, 5, 6, 7, 8, and 9 in rat neurons and glia in vitro. *Virology* **372,** 24–34 (2008).

29. Peviani, M. *et al.* Lentiviral vectors carrying enhancer elements of Hb9 promoter drive selective transgene expression in mouse spinal cord motor neurons. *J. Neurosci. Methods* **205,** 139–147 (2012).

30. Palmer, A. E., Jin, C., Reed, J. C. & Tsien, R. Y. Bcl-2-mediated alterations in endoplasmic reticulum Ca2+ analyzed with an improved genetically encoded fluorescent sensor. *Proc. Natl. Acad. Sci. U. S. A.* **101,** 17404–17409 (2004).

31. Rizzuto, R., De Stefani, D., Raffaello, A. & Mammucari, C. Mitochondria as sensors and regulators of calcium signalling. *Nat. Rev. Mol. Cell Biol.* **13,** 566–578 (2012).

32. Filadi, R. *et al.* Presenilin 2 Modulates Endoplasmic Reticulum-Mitochondria Coupling by Tuning the Antagonistic Effect of Mitofusin 2. *Cell Rep.* **15,** 2226–2238 (2016).

33. Carriedo, S. G., Yin, H. Z. & Weiss, J. H. Motor neurons are selectively vulnerable to AMPA/kainate receptor-mediated injury in vitro. *J. Neurosci.* **16,** 4069–4079 (1996).

34. Tsang, Y. M., Chiong, F., Kuznetsov, D., Kasarskis, E. & Geula, C. Motor neurons are rich in non-phosphorylated neurofilaments: Cross- species comparison and alterations in ALS. *Brain Res.* **861,** 45–58 (2000).

35. Rao, S. D. & Weiss, J. H. Excitotoxic and oxidative cross-talk between motor neurons and glia in ALS pathogenesis. *Trends in Neurosciences* **27,** 17–23 (2004).

36. Stutzmann, G. & Mattson, M. Endoplasmic Reticulum Ca2+ Handling in Excitable Cells in Health and Disease. *Pharmacol. Rev.* **63,** 700–727 (2011).

37. Verkhratsky, A. & Toescu, E. C. Endoplasmic reticulum Ca^{2+} homeostasis and neuronal death. *J Cell Mol Med* **7,** 351–361 (2003).

38. Sambrook, J. & W Russell, D. Molecular Cloning: A Laboratory Manual. *Cold Spring Harb. Lab. Press. Cold Spring Harb. NY* 999 (2001).

39. Gurney, M. E. *et al.* Motor neuron degeneration in mice that express a human Cu,Zn superoxide dismutase mutation. *Science* **264,** 1772–5 (1994).

40. Mettling C, et al. Survival of Newly Postmitotic Motoneurons Is Transiently Independent of Exogenous Trophic Support. **75,** 3128–3137 (1995).

41. De Mario, A. *et al.* The prion protein constitutively controls neuronal store-operated Ca(2+) entry through Fyn kinase. *Front. Cell. Neurosci.* **9,** 416 (2015).

42. Martorana, F. *et al.* The BH4 domain of Bcl-X L rescues astrocyte degeneration in amyotrophic lateral sclerosis by modulating intracellular calcium signals. *Hum. Mol. Genet.* **21,** 826–840 (2012).

43. Foust, K. D. *et al.* NIH Public Access. **27,** 59–65 (2010).

44. Tanguy, Y. *et al.* Systemic AArh10 provides higher transgene expression than AAV9, in the brain and the spinal cord of neonatal mice . *Frontiers in Molecular Neuroscience* **8,** (2015).

4.7 Legends to Figures

Figure 1. The cameleon probes under the control of the Hb9-derived promoter are expressed in differentiated, but not in non-differentiated, NSC-34 MN cells. NSC-34 cells were infected with the AAV vectors coding for the Hb9_AB-driven cameleon probes targeted to the cytosol (D1cpv, panels A-D), the mitochondrial matrix (4mtD3cpv, panels E-H), or the ER lumen (D4ER, panels I-L), and then cultured (7 days) under non-differentiating (proliferating, panels A,B,E,F,I,J) or differentiating (by growth in the presence of retinoic acid 5 μM, panels C,D,G,H,K,L) conditions. Fluorescence (λ_{ex} = 488 nm, λ_{em} = 526/550 nm) and differential interference contrast (DIC) micrographs of representative fields were taken with a suitable microscope equipped with a CCD camera. No fluorescent cell was observed in non-differentiated NSC-34 cultures, while the fluorescent Ca^{2+} probes were expressed in cells differentiated towards a MN phenotype. Shown data are representative of at least 3 independent experiments yielding comparable results. Scale bar = 20 μm.

Figure 2. The cameleon probes are selectively expressed in motor neurons in mouse spinal cord primary cultures. Primary cell cultures from the spinal cord of Tg mice expressing hSOD1(WT) were transduced with the AAV vectors coding for the cameleons targeted to the cytosol (panels A-D), the mitochondrial matrix (panels E-H) or the ER lumen (panels I-L). After 12 days of culturing, cells were fixed, permeabilised, immunostained with an antibody to the MN marker SMI32, and then counter-stained with the nuclear fluoro-probe Hoechst 33342.
Confocal microscope images of cells were then collected after excitation at either λ = 488 nm for visualising the fluorescent Ca^{2+} probes (green signal, panels A,E,I), λ = 543 nm for visualising SMI32-positive cells (red signal, panels B,F,J), or λ = 405 nm for visualising the nuclei of all cells (blue signal, panels C,G,K). Merging of the three fluorescent channels (panels D,H,L) shows that only SMI32-positive MNs express the Ca^{2+}probes. Similar results were obtained using hSOD1(G93A)-expressing Tg mice (Data not shown). Scale bar = 20 μm.

Figure 3. The cameleon probes correctly localize to the target sub-cellular compartment in primary MNs. Primary cell cultures from the mouse spinal cord were transduced with the AAV vectors coding for the cameleons targeted to the cytosol (panels A-C), the mitochondrial matrix (panels D,F) or the ER lumen (panels G-I). After 12 days of culturing, cells where fixed, permeabilised, and immunostained with antibodies to proteins present in the cytosol (Hsp-90, panel B), mitochondria (Tom-20, panel E), or the ER (calreticulin, panel H). Fluorescence images of cells were then collected by a confocal microscope after excitation at either λ = 488 nm for visualising the fluorescent Ca^{2+} probes (green signal, panels A,D,G), or λ = 543 nm for visualising the

immuno-labeled proteins (red signal, panels B,E,H). Merged images (panels C,F,I) show a remarkable overlapping of the green and red signals, demonstrating the correct sub-cellular targeting of all used Ca^{2+} probes. Scale bar = 20 μm.

Figure 4. Measurements of Ca^{2+} basal levels, and Ca^{2+} transients following stimulation, in different domains of primary spinal cord MNs. Primary spinal cord cultures from hSOD1(WT) or hSOD1(G93A) were transduced with the AAV vectors coding for the cameleon probes targeted to the cytosol (panels A,B), the mitochondrial matrix (panels C,D) or the ER lumen (panels E,F). After 12 days of culturing, FRET measurements were performed on single MNs expressing the different Ca^{2+} probes using a computer-assisted fluorescence microscope equipped with a suitable system for double-wavelength excitation. The ratio (R) between the FRET acceptor and donor was calculated by the data acquisition software, allowing the comparison of Ca^{2+} mobilisation following stimulation with AMPA (25 μM in the presence of 2 mM $CaCl_2$, for the cytosol and the mitochondrial matrix) or caffeine (100 μM, for the ER) at the time-points indicated by arrows, between hSOD1(WT) or hSOD1(G93A) MNs. Panels A,C,E report average traces of the Ca^{2+} dynamics (for seek of clarity error bars are not reported), while bar diagrams of panels B,D,F report the mean difference between FRET ratios ($\Delta R = R_{peak} - R_{baseline}$) following the indicated stimulus in the three cell compartments. While no difference was recorded in Ca^{2+} movements in the mitochondrial matrix or the ER lumen, the cameleon-based approach highlighted a significantly higher Ca^{2+} response following AMPA stimulation in the cytosol of hSOD1-G93A-expressing MNs compared to the hSOD1-WT counterpart. Data are reported as mean ± standard error of the mean (SEM); n = 6 (A and B), 12 (C and D), 9 (E and F); * $p < 0.01$, Student's t-test.

Figure 5. The MN promoter-driven cameleons can be efficiently and specifically expressed in MNs after *in vivo* transduction of mice with the AAV vectors. Neonatal (P1) hSOD1(WT)-expressing Tg mice were injected into the temporal vein with AAV vectors encoding the mitochondrial (panels A-C) or the ER (panels D-I) cameleon. Mice were sacrificed 4 weeks after injection, and spinal cord cross-sections were stained with the nuclear fluorescent dye Hoechst 33342 and observed with a fluorescence stereo-microscope (panels A-F) or an inverted fluorescence microscope (panels G-I). Low-resolution stereo-microscopy shows a diffuse expression of both fluorescent Ca^{2+} probes (green signal), indicating that the cameleons are effectively transduced and expressed in the spinal cord *in vivo*. The higher resolution provided by the fluorescence microscope shows that the signal of the ER cameleon is only present (to different extent) in cells resembling the morphology of large MNs (arrowheads in panel I), suggesting the cell-specific expression of the probe. Scale bars = 200 μm (A-C), 150 μm (D-F), 10 μm (G-I).

4.8 Figures

Figure 1.

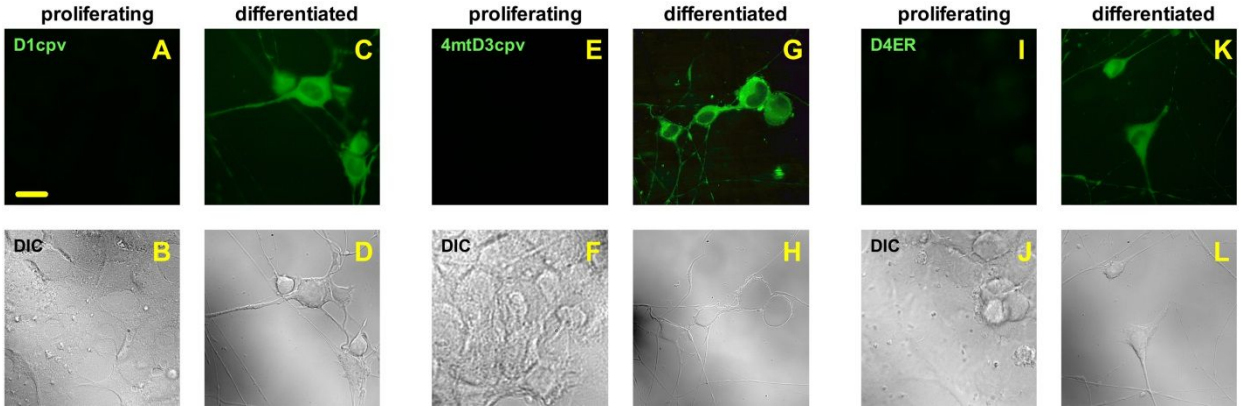

Figure 2.

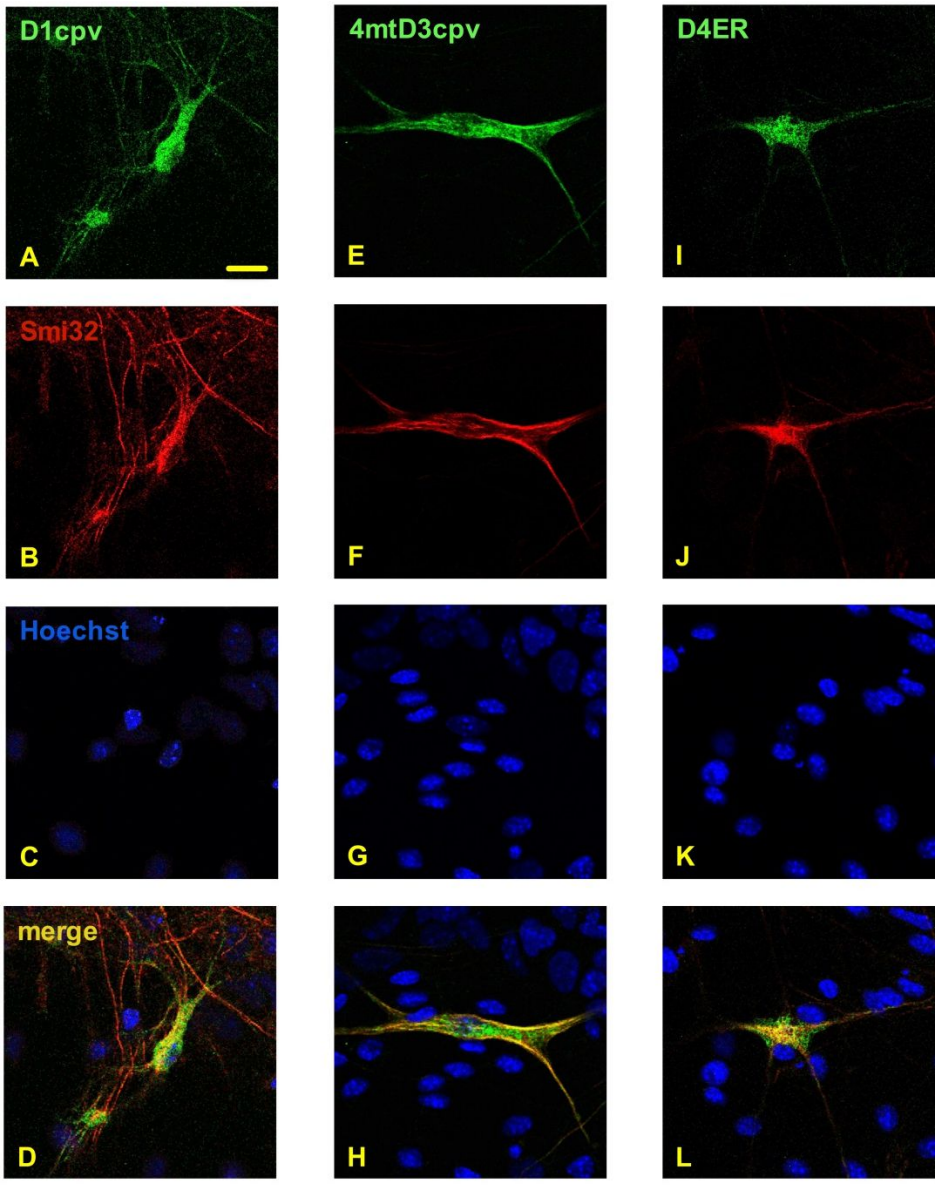

Figure 3.

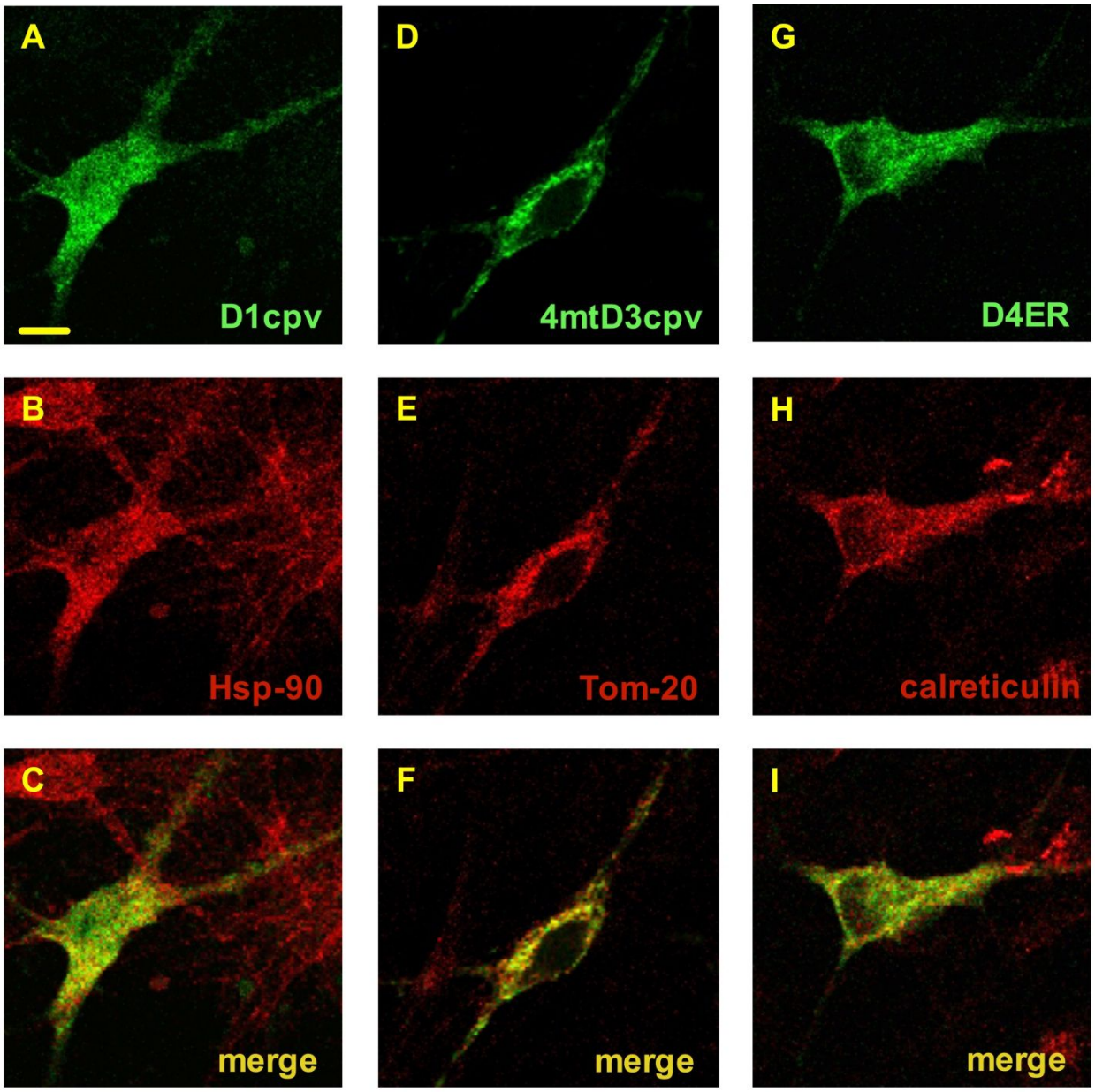
A
D1cpv
D
4mtD3cpv
G
D4ER
B
Hsp-90
E
Tom-20
H
calreticulin
C
merge
F
merge
I
merge

Figure 4 .

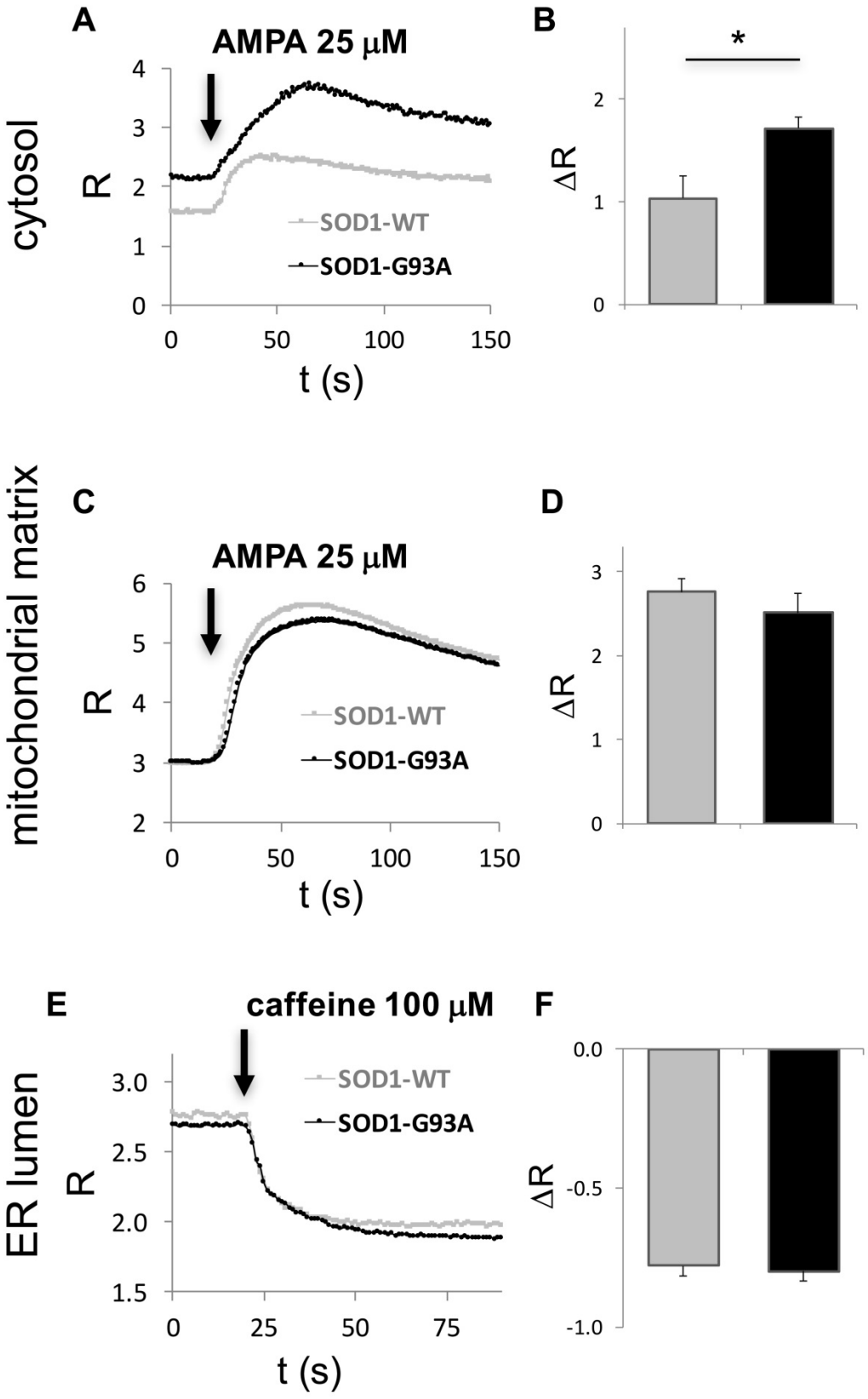
A
AMPA 25 μM
cytosol
R
SOD1-WT
SOD1-G93A
t (s)
B
*
ΔR
C
AMPA 25 μM
mitochondrial matrix
R
SOD1-WT
SOD1-G93A
t (s)
D
ΔR
E
caffeine 100 μM
ER lumen
R
SOD1-WT
SOD1-G93A
t (s)
F
ΔR

Figure 5.

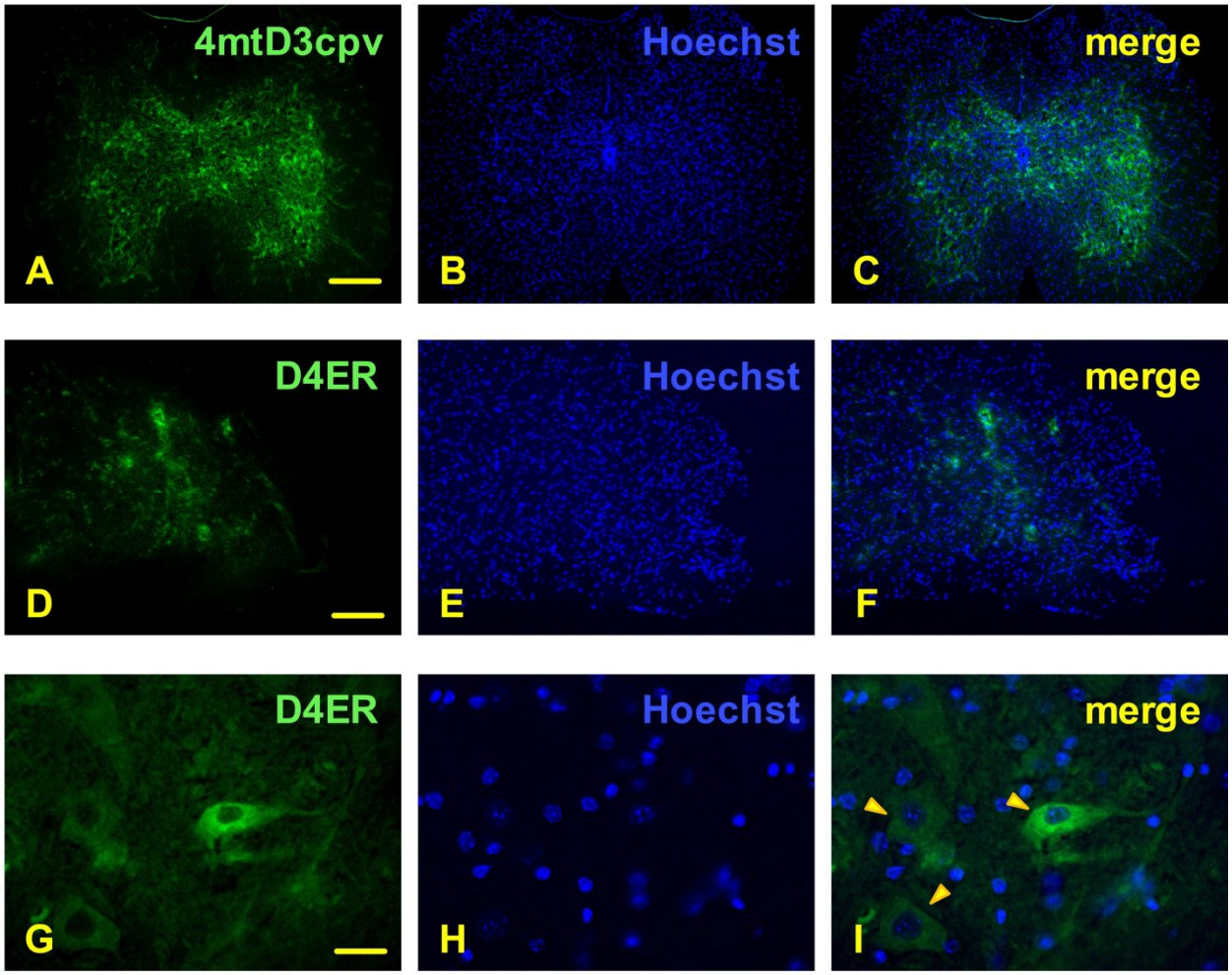
4mtD3cpv
Hoechst
merge
A
B
C
D4ER
Hoechst
merge
D
E
F
D4ER
Hoechst
merge
G
H
I

5. Local Perturbations of Ca^{2+} Homeostasis in Spinal Astrocytes as Possible Mechanisms of fALS Pathogenesis

Rosa Pia Norante[1], Maria Lina Massimino[2], Paolo Lorenzon[1§], Agnese De Mario[1], Maria Catia Sorgato[1,2], Alessandro Bertoli[1*]

[1]Department of Biomedical Science, University of Padova, Italy
[2]CNR Neuroscience Institute, Padova, Italy

[§]Current address: Department of Integrative Medical Biology (IMB), Umeå Universitet, 901 87 Umeå, SE

[*]To whom correspondence should be addressed:
Alessandro Bertoli, Dept. of Biomedical Science, University of Padova
Via U. Bassi 58/B, 35131 Padova, Italy
Tel: +39 049 8276150
Fax: +39 049 827 6363
E- mail: alessandro.bertoli@unipd.it

Contributions of authors
All authors contributed to this work. R.P.-N., M.L.-M., A.-D.M., and A.B. conceived and designed the experiments; R.P.-N., M.L.-M., and A.-D.M. performed the experiments; R.P.-N., M.L.-M., and A.B. analysed data and wrote the manuscript; M.C.-S. reviewed the manuscript.

5.1 Abstract

Amyotrophic lateral sclerosis (ALS) is a fatal neurodegenerative disorder characterised by the selective damage and death of motor neurons (MNs), probably by a combination of cell- and non-cell-autonomous processes. The past decades have brought many important insights into the role of astrocytes in normal nervous system function and disease, and there is evidence suggesting that they play a key part in MN demise in ALS. In addition, recent studies suggested a fundamental implication of perturbed Ca^{2+} homeostasis in the pathogenesis of this neurodegenerative disorder and, possibly, also in MN-astrocyte cross-talk in ALS.

These observations prompted us to investigate Ca^{2+} homeostasis and the expression of major systems involved Ca^{2+} metabolism in different cells compartment of primary spinal astrocytes derived from the hSOD1(G93A) ALS mouse model in comparison with the hSOD1(WT)-expressing controls.

Following previous results from other groups, we found that store-operated Ca^{2+} entry – a cell Ca^{2+}-refilling mechanism responsive to endoplasmic reticulum (ER) Ca^{2+} depletion – is significantly enhanced in SOD1(G93A). We also observed that stimulation of purinergic receptors induces an excess of Ca^{2+} release from the ER stores in SOD1(G93A) astrocytes. We provide possible mechanistic explanation for these results.

5.2 Introduction

ALS is an adult-onset MN disease that mainly develop on sporadic grounds, but can also be induced by autosomal mutations in different genes. Such mutations determine MN demise by both cell autonomous and non-cell-autonomous events. Important insights on the pathogenic mechanisms came from studies in mice expressing ALS-related mutant (m) forms of human (h) superoxide dismutase 1 (SOD1). This studies have shown that non-neuronal cells (e.g., glial cells and skeletal myocytes) may substantially contribute to mSOD1-associated MN damage by *in-trans* mechanisms. Following the seminal work by Cleveland and colleagues[1–3], for example, many pieces of evidence have underscored that altered astrocytic signalling, including Ca^{2+} dysmetabolism, disrupts MN functions and viability in different ALS models[4–9].

In this context, it worth noting that astrocytes, the most abundant non-neuronal cells surrounding MNs, have a pivotal role in the maintenance of neuronal metabolism, by releasing neurotrophic factors and sequestering glutamate from the synaptic cleft, thereby protecting neurons from glutamate excitotoxicity. Several *in vivo* and *in vitro* studies revealed many pathogenic changes in ALS astrocytes, including disrupted Ca^{2+} homeostasis[10], suggesting that altered astrocytic functions and/or release of different (neurotoxic) molecules by astrocytes concur to MN death[11]. Therefore, clarifying (Ca^{2+}-dependent) ALS-associated alterations of the astrocyte-MN cross-talk may help understanding pathogenic pathways and devising novel therapeutic targets.

To get insights into these issue, we studied possible alterations of local Ca^{2+} homeostasis in primary astrocytes from the murine SOD1(G93A) ALS model, following stimulation of store-operated Ca^{2+} entry (SOCE) or purinergic receptors by adenosine triphosphate (ATP).

Thanks to the fact that primary astrocytes from spinal cord of newborn mice can be easily obtained with high purity and transduced with expression vectors, we were able to perform comparative analyses on astrocytes expressing the ALS-related hSOD1(G93A) mutant and the wild-type (WT) counterpart. In particular, for the analysis of Ca^{2+} transients we used aequorins (AEQs) that allowed measuring Ca^{2+} concentrations in different cellular compartments, thanks to suitable targeting sequences.

In recent years SOCE has been proposed as an important mechanism of cell Ca^{2+} entry, distinguished from that mediated by canonical voltage- or ligand-gated channels. It has been described to occur upon intracellular Ca^{2+} store depletion that leads to the opening of store-operated Ca^{2+} channels (SOCCs), allowing external Ca^{2+} entry in the cells through the plasma membrane (PM) and replenishment of the endoplasmic reticulum (ER) Ca^{2+} stores. This “new” type of Ca^{2+}

channel was first described in non-neuronal cells (e.g., lymphocytes), but its importance is now becoming increasingly recognized also in neurons, whereby it could play a role in excitability.

The first description of SOCE (also called capacitive Ca^{2+} entry) was forwarded by Bird *et al.* (1993)[12], who reported that sarco/endoplasmic reticulum Ca^{2+}-ATPase (SERCA) inhibitors (e.g., thapsigargin) elicited Ca^{2+} entry from the extra-cellular space with no need of activating the typical cell surface channels. Only 20 years later, however, the molecular mechanisms of SOCE were eventually discovered thanks to the identification and cloning of two protein families: the ER stromal interaction molecules (STIM) (with STIM1 and STIM2 isoforms), and that of the PM ORAI proteins (with ORAI1-3 isoforms)[13,14].

Astrocytes exhibit elevated intracellular Ca^{2+} levels in response to SOCE activation, and some finding suggests an enhanced S-glutathionylation of STIM1 and aberrant SOCE and ER Ca^{2+} filling in mutant hSOD1(G93A) astrocytes[15].

In the second part of this work we analysed astrocytic Ca^{2+} fluxes following purinergic stimulation. Purinergic receptors are a family of PM proteins divided into two large families: ligand-gated ion channels (P2X ionotropic receptors) and G-protein coupled receptors (P1 and P2Y metabotropic receptors). The first ones are non-selective cation channels that mediate entering of Ca^{2+} ions from the extra-cellular space as a response to ATP stimulation. The second class of receptors can be distinguished on the basis of ligand recognition: P1 receptors are selectively activated by adenosine, while P2Y receptors are preferentially activated by ATP. Considering that one of the most important achievements in the field of purinergic transmission was the demonstration that in the brain intercellular communication is also mediated by ATP P2 receptor activation on astrocytes[16], we hypothesize that this nucleotide-induced activation may act as a defence mechanism to protect neurons, but its dysregulation in disease can lead to chronic inflammatory processes and neuronal cell damage and death, such as those occurring in ALS.

Our study has underlined altered Ca^{2+} homeostasis in different cellular compartments of spinal hSOD1(G93A) astrocytes after the above-described stimulation protocols, which is likely correlated to a different expression of some Ca^{2+}-transporting systems. Our data thus confirm and extend previous experimental evidence reporting enhanced S-glutathionylation of STIM1 and aberrant SOCE and ER Ca^{2+} filling in hSOD1(G93A) astrocytes[15]. We also propose a novel mechanism for the specific role of P2 receptors in astrocytes (enhanced Ca^{2+} release from the ER upon ATP stimulation) that may provide the basis for neuroprotective strategies.

5.3 Results and Discussion

5.3.1 hSOD1(G93A)-expressing astrocytes have enhanced SOCE-mediated Ca^{2+} influx

Considering that astrocytes have a well-recognised pivotal role in the tripartite synapse and seems to be involved in ALS pathogenesis, and that the control of Ca^{2+} homeostasis is fundamental for the life and functions of astrocytes[5,17], we decided to study Ca^{2+} dynamics in primary spinal astrocytes from hSOD1(G93A) and hSOD1(WT) mice. Starting from a recent work suggesting oxidative stress-induced S-glutathionylation and Ca^{2+}-independent clustering of the ER Ca^{2+} sensor STIM1[15], which determine abnormal SOCE in hSOD1(G93A)-expressing murine astrocytes, we decided to perform an analysis of local Ca^{2+} homeostasis in these cells compared to the WT counterpart. Thanks to our tools, we were able to measure Ca^{2+} fluxes in different cell compartments, in order to define a more precise picture of Ca^{2+} dysmetabolism in ALS astrocytes.

We explanted primary astrocytes from the spinal cord of newborn (P 0-1) hSOD1(G93A) and hSOD1(WT) mice and, after three weeks of culture, astrocytes were re-plated and analysed for different Ca^{2+}-related parameters (Fig. 1). We obtained almost pure (>97%) cultures as determined by immunofluorescence analysis for the astrocytic marker glial fibrillary acidic protein (GFAP) (Fig. 2). Morphology did not significantly differ between the two hSOD1 genotypes astrocytes (data not shown).

Intracellular Ca^{2+} dynamics, following SOCE stimulation, were evaluated by live-cell analysis using the bioluminescence photo-protein AEQ targeted to different cell compartments (i.e., cytosolic PM micro-domains (AEQ_{pm}), bulk cytosol (AEQ_{cyt}), ER lumen (AEQ_{ER}) and mitochondrial matrix (AEQ_{mit}). To maximally activate SOCE, we firstly depleted intracellular Ca^{2+} stores (by incubation in a Ca^{2+}-free buffer containing EGTA 100 μM), and then perfused cells with 1 mM $CaCl_2$.

Fig. 3 reports Ca^{2+} fluctuations in PM micro-domains (A) and in the cytosol (B), as detected by AEQ_{pm} and AEQ_{cyt} respectively. The rise of $[Ca^{2+}]_{pm}$ (Fig. 3A) and $[Ca^{2+}]_{cyt}$ (Fig. 3B) had a significantly higher (of 30% and 25%, respectively) peak value in hSOD1(G93A) (red) than in hSOD1(WT) (black) astrocytes, indicating that hSOD1(G93A) expression leads to higher SOCE-mediated Ca^{2+} replenishment of astrocytes. These findings were confirmed by a higher Ca^{2+} uptake by the ER of hSOD1G93A astrocytes following SOCE activation (Fig.4).

The mechanism of SOCE activation involves two families of ER resident and PM proteins, which are STIM1-2, and ORAI1-3, respectively[18]. In particular, STIM1 and 2 sense luminal Ca^{2+} changes

with different sensitivity. STIM1, whose EF-hand motif binds Ca^{2+} with low affinity (ideal to sense substantial changes of the luminal ER Ca^{2+} concentration), is uniformly distributed in the ER membrane at resting conditions, whereas it oligomerizes upon Ca^{2+} depletion in membrane *punctae* closely juxtaposed to the PM, thereby recruiting the PM channel-forming ORAI proteins, and promoting pore opening, possibly through protein-protein interaction[14,19]. Conversely, STIM2 is sensitive to mild reductions of ER Ca^{2+} concentration, so that STIM2 could form PM-recruiting *punctae* already at resting ER Ca^{2+} concentrations[20,21].

To determine whether enhanced SOCE in hSOD1(G93A) astrocytes was attributable to increased expression of the components of the SOCE molecular mechanism, we evaluated by Western blot (WB) the expression of STIM1, STIM2, ORAI1 and ORAI3 (ORAI2 is under analysis), but no significant difference was observed (Fig. 5). Following the findings by *Kawamata et al.* (2014)[15] demonstrating that STIM1 S-glutathionylation is responsible for abnormal SOCE in hSOD1(G93A) primary spinal cord astrocytes, we confirmed the enhancement of total proteins S-glutathionylation in the same ALS cell paradigm (data not shown), supporting the contention that increased SOCE could be due to Ca^{2+}-independent STIM1-containing *puncta* formation.

The maintenance of proper intracellular Ca^{2+} concentrations is guaranteed by an efficient network of Ca^{2+}-transporting pathways and by Ca^{2+}-buffering proteins present in the cytosol and in the lumen of intracellular Ca^{2+}-storing compartments[22]. The ER is generally believed to be the most important, metabolically relevant, reservoir and buffering compartment for cellular Ca^{2+}. The ER lumen contains high Ca^{2+}concentration and several Ca^{2+}-binding proteins[23], and fluctuations of $[Ca^{2+}]_{ER}$ may affect Ca^{2+}-dependent processes both in the lumen of the organelle and in other cell compartments (e.g., changes in cytosolic and mitochondrial Ca^{2+} levels that might affect numerous signal transduction pathways)[24].

Considering that the mechanisms controlling Ca^{2+} storage in the ER are key to cell Ca^{2+} homeostasis, and that many severe diseases result from impaired function of the ER membrane or ER Ca^{2+} binding proteins, we analysed by WB the expression of Ca^{2+}-binding proteins or Ca^{2+}-transporting systems. Although Ca^{2+}-binding proteins such as calreticulin (CRT), calnexin (CLNX) and GRP78 did not show significant differences between the two hSOD1 genotypes (Fig.6A-C), we found that sarco-endoplasmic reticulum (SERCA, Fig.6D) and PM Ca^{2+} ATPases (PMCA, Fig. 6E) are overexpressed in hSOD1(G93A) astrocytes compared to the hSOD1(WT) counterpart.

These findings might well correlate with SOCE dysregulation and altered cytosolic and ER Ca^{2+} levels. Indeed, increased SERCA levels could not be sufficient to restore normal resting ER Ca^{2+}

levels in hSOD1(G93A) astrocytes in light of the notion that PMCA overexpression might cause an overall reduction of cell (and ER) resting Ca^{2+} concentrations[25].

It is largely accepted that mitochondria play a critical role in buffering cell Ca^{2+} by actively taking up the ion in the mitochondrial matrix through the recently discovered mitochondrial Ca^{2+} uniporter (MCU) complex located in the inner mitochondrial membrane, and thanks to the sustained mitochondrial membrane potential ($\Delta\psi_m$)[26]. Furthermore, mitochondrial dysfunctions (also in astrocytes) were repeatedly correlated to ALS pathogenesis[6,27,28]. In light of this notion, we controlled the calcium uptake capability of mitochondria after SOCE stimulation in primary spinal cord astrocytes of hSOD1(G93A) and hSOD1(WT) mice (Fig. 7). No difference was found between hSOD1(G93A) and hSOD1(WT) primary spinal cord astrocytes, which is leading to assume that mitochondrial calcium uptake does not contribute to excess cytosolic calcium concentration after SOCE stimulation in hSOD1(G93A).

Subsequently, because $\Delta\psi_m$ is the driving force for mitochondrial Ca^{2+} uptake, we compared $\Delta\psi_m$ using the potentiometric probe tetra-methylrhodamine methyl ester perchlorate (TMRM) (a cell-permeant, cationic, red-orange fluorescent dye that is readily sequestered by active mitochondria), in primary spinal cord astrocytes of hSOD1(G93A) and hSOD1(WT) mice (Fig. 8). The fluorescence signal of TMRM can be directly correlated to $\Delta\psi_m$ across the inner mitochondrial membrane[29]. We found that hSOD1(G93A) astrocytes do not show significant variations in $\Delta\psi_m$, suggesting no bioenergetic abnormalities ALS astrocytes (Fig.8 A-B).

We also analysed some other mitochondrial parameters, such as the mitochondrial morphology an distribution and the expression of the MCU Ca^{2+} uniporter (Fig. 9, Fig. 10). Mitochondrial morphology was quantified in cells ectopically expressing the mitochondrial red fluorescent protein mtRFP (Fig. 9A). Evaluation of mitochondria circularity (index of elongation) revealed no difference between the two hSOD1 genotypes.

MCU is a calcium transporter that localizes to the mitochondrial inner membrane and allows the mitochondrial uptake of calcium ions: in our experimental setting, no different was observed between hSOD1(G93A) and hSOD1(WT) astrocytes (Fig. 10). It is worth noting, however, that the complex regulation of MCU activity, implicating other complex subunits (i.e., MICU1-2, EMRE) demands for further analysis on this topic.

Together, these results indicate that mitochondria play a minor role, if any, in regulating cell Ca^{2+} levels, and that no abnormality in mitochondrial bioenergetics, morphology and MCU expression occurs in primary spinal cord astrocytes carrying the ALS-related hSOD1(G93A) mutant.

In summary, the above results demonstrate that hSOD1(G93A)-expressing astrocytes have enhanced SOCE-mediated Ca^{2+} influx from the extracellular space into the cytosol and the ER lumen, most probably due to increased formation of STIM1 *punctae* at the PM[15]. This mechanism is also associated the SERCA over-expression of in hSOD1(G93A) astrocytes, which – however – is not sufficient to counteract ER basal Ca^{2+} depletion, possibly because increased PMCA expression functionally predominates[25]. In this scenario, mitochondria seem to have a minor role in regulating cytosolic Ca^{2+} levels after SOCE stimulation in hSOD1(G93A) and control astrocytes.

5.3.2 Increase of Ca^{2+} release from the ER after ATP stimulation

An important role in cell Ca^{2+} homeostasis of the nervous system is played by G-protein-coupled receptors (GPCRs), among which purinergic receptors are important regulators of neuronal development in the context of the neuron-glia interplay. For instance, GPCR activation on the PM is the major mechanism increasing cytosolic Ca^{2+} levels in astrocytes thanks to the activation of inositol trisphosphate (IP_3) receptors (IP_3Rs) on the ER membrane and consequent Ca^{2+} release from the ER[30].

They express P2Y1, P2Y2, P2Y4, P2Y6, P2Y12, and P2Y14 metabotropic GPCRs[31], but the signalling pathways controlled by these receptors are not completely understood. In light of the increased Ca^{2+} release from the ER during ATP stimulation reported in in hSOD1(G93A) astrocytes by Kawamata *et al.* (2014)[15], we have focused our attention on astrocytic Ca^{2+} dynamics upon activation of purinergic receptors.

Intracellular Ca^{2+} dynamics were evaluated by live-cell imaging, using AEQs targeted to the cytosol or the mitochondrial matrix and expressed by lentiviral vector systems, in response to purinergic receptor activation by ATP. We observed comparable Ca^{2+} transients in both cell compartments following stimulation with ATP in a Ca^{2+} (1 mM)-containing (data not shown) or a Ca^{2+}-free medium (Fig.11 A,B), indicating that intracellular Ca^{2+} movements were caused by IP_3R activation and release of the ion from the ER rather than entry from the extra-cellular space through ionotropic receptors. Such Ca^{2+} transients were higher in the cytosol of hSOD1(G93A) than in hSOD1(WT) astrocytes (Fig.11A), while – quite surprisingly – no difference was observed in the mitochondrial matrix (Fig.11B).

To mechanistically explain this increase in ER Ca^{2+} release after ATP stimulation we performed preliminary experiments to estimate the expression of IP_3R and some metabotropic purinergic receptors present in astrocytes. No significant difference was observed in IP_3R and P2Y1 (Fig.12A, B), while P2Y6 is much more abundant in hSOD1(G93A) astrocytes than in hSOD1(WT) cells (Fig.12C). Given that this receptor is preferentially activated by UDP rather than ATP, other experiments are in progress, in which we are testing UDP or different ATP concentrations to stimulate astrocytes.

Thus, to thoroughly investigate and better explain the molecular pathways that are behind these alterations in Ca^{2+} metabolism and protein expression, different approaches are presently being performed, including ATP dose-response experiments and dosing of IP_3 in astrocytes with the two

hSOD1 genotypes. This last part of the work, however, is still in progress, and all hypotheses are not yet confirmed by statistical analyses.

We want also try to restore Ca^{2+} peak value in hSOD1G93A astrocytes with a dosing of ATP stimulus in attempt to find a possible target for molecular drugs. These investigations will be complemented with by pharmacological approaches on Purinergic Receptor to assess whether their inhibition perturbs the overall astrocyte Ca^{2+} homeostasis in a way that depends on mSOD1 expression.

The exact mechanisms by which mutant SOD1 is toxic to MNs are not yet defined. *In vitro* ALS models, however, disclosed that expression of SOD1(G93A) in astrocytes induces extensive death of co-cultured spinal cord MNs[11]. Accordingly, primary MNs are also sensitive to the treatment with conditioned medium from astrocytes expressing mutant SOD.

On the other hand, astrocytes form tripartite synapses with presynaptic and postsynaptic neuronal terminals, and actively modulate neuronal/synaptic functions by releasing (by Ca^{2+}-regulated mechanisms) gliotransmitters such as glutamate, ATP, and D-serine. It is also recognized that, in ALS, astrocytes undergo a series functional alterations leading MNs to irrecoverable degeneration.

For all this reasons, our findings of local Ca^{2+} dysregulation upon SOCE and purinergic stimulation in SOD1(G93A) astrocytes could pave the way to the understanding of cell mechanisms related to MN damage, and the identification of new biological targets for the development of therapeutical strategies.

5.4 Materials and Methods

5.4.1 Animals & Mouse genotyping

Please refer to "Animals" and "Mouse genotyping" in the previous part "Generation and validation of novel adeno-associated viral vectors for the analysis of Ca^{2+} homeostasis in motor neurons".

5.4.2. Primary cultures

Primary cultures of spinal astrocytes were isolated from newborn mice and cultured as described in Martorana *et al*. (2012)[7]. Briefly, after extraction and dissection in Hank's Buffer (Sigma), spinal cord was incubated (5', 37°C) in the same solution added with Collagenase (0.25%). Threw the supernatant, the pellet was re-suspended in Hank's Buffer with DNase (0.05%), mechanically dissociated, added with minimal essential medium (MEM, Gibco) supplemented with FBS 10% (v/v) and centrifuged (220 g, 5'). The pellet was re-suspended in complete medium [MEM supplemented with FBS 20% (v/v), L-glutamine 2 mM, glucose in phosphate buffered saline (PBS) 0.3% (w/v), penicillin 100 U/ml, streptomycin 100 µg/ml] and seeded. Once the cultures reached the confluence (three weeks), they were re-plated at the optimal density 80.000 cells/well in 24-well plates (AEQ_{cyt}, AEQ_{mt} and AEQ_{pm} measurements) or 160.000 cells/well in 12-well plates (cameleon measurements) containing glass coverslips and maintained in complete medium. For AEQ_{ER} measurements cells were re-plated at the optimal density 12.000 cells/well in 96-well plates and maintained in the same medium.

Cultures purity was proved by immunocytochemical test and was at (at least) >97% .

Lentiviral particles (see below for the production), AEQ_{pm}, AEQ_{cyt}, AEQ_{mt} and AEQ_{ER}, were added to astrocytes 24 h after plating and after further 72 h were used for experiments.

5.4.3 Immunocytochemistry

For immunocytochemical analysis, astrocytes (96h in vitro) were firstly washed in ice-cold PBS, and then fixed (20 min, RT) in paraformaldehyde [PFA, 4% (w/v)] in PBS. After washing in PBS, cells were permeabilized in PBS containing Triton X-100 [1 h, RT, 0.02% (w/v)] and then incubated (overnight, 4 °C) with rabbit anti-GFAP polyclonal (p) Ab (1:500, Dako) and mouse anti-HA monoclonal (m) Ab (1:500, Covance). After extensive washings in PBS, cells were incubated (1 h, 37 °C) respectively with the secondary antibodies rhodamine-conjugated anti-rabbit IgG (1:100, Dako) and Alexa Fluor 555-conjugated anti-mouse IgG (1:500, Molecular Probes). Cell nuclei were counter-stained with Hoechst 33342 (5 µg/ml, Sigma), and coverslips were finally

washed in PBS, mounted in montage solution [8% Mowiol 40-88 (Sigma) in glycerol and PBS (1:3 (v/v)], and observed with an inverted fluorescence microscope (Leica CTR6000) equipped with a computer-assisted charge-coupled camera (Orca Flash 4.0, Hamamatsu), or with a confocal microscope system (Leica TCS-SP5), which also allowed the acquisition and analysis of digital images.

5.4.4. Construction of lentiviral vector

To follow Ca^{2+} fluctuations in specific astrocytes compartments, we exploited a lentiviral expression system to transduce cells with chimeric constructs encoding the Ca^{2+}-probe aequorin (AEQ) tagged with the influenza virus hemagglutinin (HA) epitope, and linked to sequences addressing the protein to the cytosolic domains proximal to the PM (AEQ_{pm})[32], the cytosol (AEQ_{cyt})[33], the ER lumen (AEQ_{ER})[34], and the mitochondrial matrix (AEQ_{mt})[35]. Lentiviral vectors for AEQ_{pm}, AEQ_{ER} and AEQ_{mt} were generated as described[36,37], using an AEQ mutant with reduced Ca^{2+} affinity that allows measurements of $[Ca^{2+}]$ >10 μM[38].

Conversely, to detect variations of cytosolic $[Ca^{2+}]$, a chimeric construct of WT AEQ fused to the monomeric red fluorescent protein (mRFP) was used. To generate the AEQ_{cyt} lentiviral vector, two PCR reactions were performed. In the first PCR, the mRFP sequence was amplified without the stop codon using the pCDNA3-mRFP plasmid (Clontech) as template, and the following primers:

XbaI-mRFP (forward, CGTCTAGAATGGCCTCCTCCGAGGAC)

mRFP-BglII (reverse, GAGGCGCCGGTGGAGTGGAGATCTCG)

In the second PCR, the HA-AEQ cassette was amplified using the pCDNA1-AEQcyt plasmid[33] as template, and the following primers:

BglII-AEQ (forward, CGAGATCTCGAGCTCAAGCTTTATGA)

AEQ-SalI (reverse, GGTATCGATAAGCTTGATGTCGACGC).

PCR products were digested with XbaI and BglII for mRFP and with BglII and SalI for HA-AeQ, and the resulting fragments were assembled into the XbaI- and SalI-digested backbone of the lentiviral vector pRRLsin.PPTs.hCMV.GFP.pre, in a three-step ligation reaction.

Lentiviral particles were produced as described in Ramezani *et al.* (2002)[39]. Briefly, HEK293T packaging cells (2 x 10^6 cells in 100 mm culture plates), cultured in Dulbecco's modified Eagle's medium (Sigma) supplemented with FBS 10%, L-glutamine 2 mM, penicillin 100 U/ml,

streptomycin 100 µg/ml (Euroclone), were co-transfected (24 h after plating), by means of the calcium-phosphate transfection method, with plasmids:

- pMD2.VSVG encoding for the envelope pseudo-typing;
- pMDLg/pRRE packaging plasmid that includes gag, coding for the virion main structural proteins, and pol, responsible for the retrovirus-specific enzymes;
- pRSV-REV, Rev cDNA expressing plasmid in which the joined second and third exons of HIV-1 rev are under the transcriptional control of RSV U3 promoter. Encoding for the protein REV for the expression of gag and pol;
- pLV-AEQ construct.

After 14 h, the transfection medium was replaced with fresh culture medium, and cells were grown for 72 h, after which the culture medium was collected. Viral particles were harvested by ultracentrifugation (50,000 g, 2 h), re-suspended in 0.2 mL of phosphate buffer saline (PBS), and stored at -80 °C until use.

5.4.5. Ca^{2+} imaging_Aequorin

All experiments with AEQ_{pm}, AEQ_{cyt} and AEQ_{mt} were performed by means of a computer-assisted luminometer equipped with a perfusion system (1). For AEQ_{ER} was used EnVision™ Multilabel Plate Reader (Perkin Elmer) (2). Depending on the type of measurement, cells were treated as described follow.

1. To measuring Ca^{2+} movements elicited by SOCE with AEQ_{pm}, AEQ_{cyt} and AEQ_{mt}, astrocytes were incubated (1 h, 37 °C, 5% CO_2) in a modified Krebs-Ringer buffer [(KRB, NaCl 125 mM, KCl 5 mM, Na_3PO_4 1 mM, $MgSO_4$ 1 mM, glucose 5.5 mM, HEPES 20 mM (pH 7.4)] supplemented with EGTA (100 µM, to deplete Ca^{2+} from cells), and coelenterazine (5 µM, Santa Cruz). After transferring the cell-containing coverslip to the thermostatted chamber of the luminometer, experiments started by perfusing cells with KRB, first containing EGTA (100 µM), then $CaCl_2$ (1 mM).

   To monitor Ca^{2+} fluxes elicited by activation of purinergic receptor with AEQ_{cyt} and AEQ_{mt}, astrocytes were incubated (1 h, 37 °C, 5% CO_2) in a modified KRB supplemented with $CaCl_2$ (1 mM), and coelenterazine (5 µM). After transferring the cell-containing coverslip to the thermostatted chamber of the luminometer, experiments started by perfusing cells with KRB, first containing EGTA (100 µM), then ATP (100 µM) with/o $CaCl_2$ (1 mM).

2. When measuring $[Ca^{2+}]$ER, astrocytes were washed three times with KRB supplemented with EGTA (1 mM), left 10 min at 37 °C (CO_2 5%), and incubated (1 h, 4 °C) in KRB supplemented with ionomycin (5 μM, Sigma), EGTA (500 μM) and a modified coelenterazine (coelenterazine n, 5 μM, Sigma), whose reduced Ca^{2+} affinity allows detection of high $[Ca^{2+}]$ER, in the end washed three times with KRB supplemented (in sequence) with: EGTA (500 μM); 2% (w/v) BSA and EGTA (1 mM) ; EGTA (500 μM). After transferring the plate into EnVision™ Multilabel Plate Reader (Perkin Elmer), experiments started by adding KRB containing $CaCl_2$ (1 mM). It is to be noted that, despite few different steps, the procedure to deplete ER Ca^{2+} store ensured that astrocytes were subjected to similar conditions to those employed when measuring $[Ca^{2+}]$ in the other tested domains before SOCE.

All experiments ended by lysing cells with digitonin (100 μM, Sigma) in a hypotonic Ca^{2+}-rich solution ($CaCl_2$ 10 mM in H_2O) to discharge the remaining AEQ pool. The light signal was digitalized and stored for subsequent analyses. Luminescence data were calibrated off-line into $[Ca^{2+}]$ values, using a computer algorithm based on the Ca^{2+} response curve of AEQ[33].

5.4.6. Measurement of mitochondrial membrane potential

The membrane potential of astrocytes mitochondria ($\Delta\psi m$) was measured using the (PM-permeable) cationic tetramethylrhodamine methyl ester probe (TMRM, λ_{exc} = 548 nm, λ_{em} = 574 nm), which accumulates electrophoretically into the mitochondrial matrix.

To analyse $\Delta\psi m$, astrocytes were incubated (30 min, 37°C, CO_2 5%) with TMRM (10nM, Molecular Probes) in KRB containing $CaCl_2$ (1 mM) and finally in Mg^{2+} free-KRB. Coverslip images were collected with an inverted microscope (Olympus IMT-2) equipped with a (75W) xenon lamp to provide fluorescence light, a 16 bit digital cooled CCD camera (provided with a cooling system Miromax, Princeton Instruments), a 40X oil objective, and appropriate excitation and emission filters. Several fields were acquired from each coverslip before and after addition of trifluorocarbonylcyanide phenylhydrazone (FCCP) (5 μM, Sigma) that, by collapsing the $\Delta\psi m$, releases the probe from mitochondria.

Images were analysed using the Image J software. Fluorescence intensity was measured in regions rich in mitochondria. For each analysed coverslip, the TMRM fluorescence intensity was calculated as the difference between the mean fluorescence intensity before and after of FCCP addition.

5.4.7. Analysis of Mitochondrial Morphology

Primary astrocytes were transiently transfected (Lipofectamine 3000, Life Technologies, according to manufacture) with mtRFP 24h after plating. After 72h cells were observed under confocal microscope system (Leica TCS-SP5) to evaluate mitochondrial morphology fluorescence. In particular, when cells exhibit a network of filamentous mitochondria usually are classified as normal (not fragmented), and cells with fragmented or partially truncated mitochondria are classified as fragmented. To calculate mitochondrial shape, fluorescence microscopy images of randomly selected fields were acquired (at least 10 fields for each coverslip), and every single mitochondrion of the investigated cells was marked to analyse morphological characteristics such as its area, perimeter, and major and minor axes. On the basis of these parameters, the mitochondrion circularity and its form factor ($4\pi \times$ area/perimeter2), consistent with a measure of mitochondrial length and the degree of branching, were calculated as described in Dagda *et al.* (2009)[40].

5.4.8. Western Blot Analysis

- *Sample preparation*

  Astrocytes, 96 hours after plating, were homogenized in a buffer containing glycerol 10% (w/v), SDS 2% (w/v), Tris/HCl 62.5 mM (pH 6.8), urea 1.8 M, $NaVO_4$ 5 mM, protease and phosphatase inhibitor cocktails (Roche), and boiled (5 min). The total protein content was determined by the Lowry method (Total Protein Kit, Micro Lowry, Peterson's Modification, Sigma), using BSA as standard. Dithiothreitol (50 mM) and bromophenol-blue (0.004% (w/v)) were added to samples just before gel loading.

- *SDS-polyacrylamide gel electrophoresis (SDS-Page) and immunoblot*

  Electrophoresis was performed on precast gels 4-15% (Bio-Rad) and run with a buffer containing 0.1 M Tris-HCl, 0.77 M glycine and 0.4% SDS, pH 8.3.

  Samples (18 μg of proteins in each lane) were run on the gel using an Electrophoresis Power Supply (BioRad), providing a constant voltage of 150 V in the stacking gel and 200 V in the separating gel. Proteins were then electro-blotted onto PVDF membranes (0.22 μm pore size, Bio-Rad). Membranes were incubated (1 h, RT) with a blocking solution of non-fat dry milk 5% (w/v), or BSA 3% (w/v) in Tris Buffer Saline added with 0.1% TWEEN 20 (w/v) (TBS-T), and followed by addition of the appropriate primary antibody (see below) (4 °C, over-night). After three 10 min-washes (with TBS-T), membranes were incubated (1 h, RT)

with a horseradish peroxidase-conjugated anti-rabbit or anti-goat IgG secondary antibody (Santa Cruz Biotechnology).

Used antibodies were (dilution in parentheses): rabbit anti-STIM1 pAb (1:1000; Cell Signaling Technology); rabbit anti-STIM2 pAb (1:1000; ProSci Inc); rabbit anti-ORAI1 pAb (1:1000; Abcam); rabbit anti-ORAI3 pAb (1:1000; Thermo Fisher Scientific); goat anti SERCA pAb (1.1000; Santa Cruz Biotechnology); rabbit anti MCU pAb (1.1000; Sigma cat.n. HPA016480); rabbit anti IP_3R pAb (1.1000; calbiochem); rabbit anti PMCA pAb (1.1000; Santa Cruz Biotechnology); rabbit anti P2Y6 pAb (1.1000; alomone labs); rabbit anti P2Y1 pAb (1.1000; Abcam), rabbit anti CRT pAb (1.1000; Abcam), rabbit anti CNX pAb (1.1000; Abcam), rabbit anti GRP78 pAb (1.1000; Abcam).

Immunoreactive bands were visualized and digitalized by means of NineAlliance (UVITEC Cambridge), using an enhanced chemiluminescence reagent kit (Millipore Corporation). For densitometric analyses, band intensities were normalized to the optical density of the corresponding lane stained with Coomassie blue.

5.4.9. Statistical analysis

For aequorin analysis values will be reported as mean ± SEM. Data analysis was performed as described in Lazzari *et al.* (2011).

Statistics for all the experiments were based on two-sample Student's t-test, with a p-value <0.05 being considered statistically significant (**$p<0.01$, ***$p<0.001$).

5.5 References

1. Clement, A. M. Wild-Type Nonneuronal Cells Extend Survival of SOD1 Mutant Motor Neurons in ALS Mice. *Science (80-.).* **302,** 113–117 (2003).

2. Yamanaka, K. *et al.* Astrocytes as determinants of disease progression in inherited amyotrophic lateral sclerosis. *Nat. Neurosci.* **11,** 251–3 (2008).

3. Ilieva, H., Polymenidou, M. & Cleveland, D. W. Non-cell autonomous toxicity in neurodegenerative disorders: ALS and beyond. *Journal of Cell Biology* **187,** 761–772 (2009).

4. Di Giorgio, F. P., Carrasco, M. A., Siao, M. C., Maniatis, T. & Eggan, K. Non-cell autonomous effect of glia on motor neurons in an embryonic stem cell-based ALS model. *Nat. Neurosci.* **10,** 608–14 (2007).

5. Bilsland, L. G., Nirmalananthan, N., Yip, J., Greensmith, L. & Duchen, M. R. Expression of mutant SOD1G93A in astrocytes induces functional deficits in motoneuron mitochondria. *J. Neurochem.* **107,** 1271–1283 (2008).

6. Cassina, P. *et al.* Mitochondrial dysfunction in SOD1G93A-bearing astrocytes promotes motor neuron degeneration: prevention by mitochondrial-targeted antioxidants. *J. Neurosci.* **28,** 4115–22 (2008).

7. Martorana, F. *et al.* The BH4 domain of Bcl-X L rescues astrocyte degeneration in amyotrophic lateral sclerosis by modulating intracellular calcium signals. *Hum. Mol. Genet.* **21,** 826–840 (2012).

8. Fritz, E. *et al.* Mutant SOD1-expressing astrocytes release toxic factors that trigger motoneuron death by inducing hyperexcitability. *J. Neurophysiol.* **109,** 2803–14 (2013).

9. Rojas, F., Cortes, N., Abarzua, S., Dyrda, A. & van Zundert, B. Astrocytes expressing mutant SOD1 and TDP43 trigger motoneuron death that is mediated via sodium channels and nitroxidative stress. *Front. Cell. Neurosci.* **8,** 24 (2014).

10. Cleveland, D. W. & Rothstein, J. D. From Charcot to Lou Gehrig: deciphering selective motor neuron death in ALS. *Nat. Rev. Neurosci.* **2,** 806–819 (2001).

11. Nagai, M. *et al.* Astrocytes expressing ALS-linked mutated SOD1 release factors selectively toxic to motor neurons. *Nat. Neurosci.* **10,** 615–22 (2007).

12. Bird, G. S. J. & Putney, J. W. Inhibition of thapsigargin-induced calcium entry by microinjected guanine nucleotide analogues: Evidence for the involvement of a small G-protein in capacitative calcium entry. *J. Biol. Chem.* **268,** 21486–21488 (1993).

13. Cabello, C. M. *et al.* NIH Public Access. **46,** 220–231 (2010).

14. Liou, J. *et al.* STIM is a Ca2+ sensor essential for Ca2+-store- depletion-triggered Ca2+ influx. *Curr. Biol.* **15,** 1235–1241 (2005).

15. Kawamata, H. *et al.* Abnormal Intracellular Calcium Signaling and SNARE-Dependent Exocytosis Contributes to SOD1G93A Astrocyte-Mediated Toxicity in Amyotrophic Lateral Sclerosis. *J. Neurosci.* **34,** 2331–2348 (2014).

16. Ceruti, S. & Abbracchio, M. P. Roles of P2 receptors in glial cells: focus on astrocytes. *Purinergic Signal.* **2,** 595–604 (2006).

17. Affairs, V. *et al.* Astrocytes and Microglia as Non-cell Autonomous Players in the Pathogenesis of ALS. **25,** 233–240 (2016).

18. Smyth, J. T. *et al.* Activation and regulation of store-operated calcium entry. *J. Cell. Mol. Med.* **14,** 2337–2349 (2010).

19. Roos, J. *et al.* STIM1, an essential and conserved component of store-operated Ca 2+ channel function. *J. Cell Biol.* **169,** 435–445 (2005).

20. Brandman, O., Liou, J., Park, W. S. & Meyer, T. STIM2 Is a Feedback Regulator that Stabilizes Basal Cytosolic and Endoplasmic Reticulum Ca2+ Levels. *Cell* **131,** 1327–1339 (2007).

21. Frischauf, I. *et al.* The STIM/Orai coupling machinery. *Channels* **2,** 261–268 (2008).

22. Corbett, E. F. & Michalak, M. Calcium, a signaling molecule in the endoplasmic reticulum? *Trends Biochem. Sci.* **25,** 307–11 (2000).

23. Meldolesi, J. & Pozzan, T. The endoplasmic reticulum Ca2+ store: A view from the lumen. *Trends Biochem. Sci.* **23,** 10–14 (1998).

24. Milner, R. E., Famulski, K. S. & Michalak, M. Calcium binding proteins in the sarcoplasmic/endoplasmic reticulum of muscle and nonmuscle cells. *Mol. Cell. Biochem.* **112,** 1–13 (1992).

25. Brini, M., Bano, D., Manni, S., Rizzuto, R. & Carafoli, E. Effects of PMCA and SERCA pump overexpression on the kinetics of cell Ca(2+) signalling. *EMBO J.* **19,** 4926–35 (2000).

26. Patron, M. *et al.* The mitochondrial calcium uniporter (MCU): Molecular identity and physiological roles. *J. Biol. Chem.* **288,** 10750–10758 (2013).

27. Coussee, E. *et al.* G37R SOD1 mutant alters mitochondrial complex I activity, Ca2+ uptake and ATP production. *Cell Calcium* **49,** 217–225 (2011).

28. Cozzolino, M. & Carri, M. T. Mitochondrial dysfunction in ALS. *Prog. Neurobiol.* **97,** 54–66 (2012).

29. Joshi, D. C. & Bakowska, J. C. Determination of mitochondrial membrane potential and reactive oxygen species in live rat cortical neurons. *J. Vis. Exp.* 2704 (2011). doi:10.3791/2704

30. C, A. *et al.* What is the role of astrocyte calcium in neurophysiology? **59,** 932–946 (2008).

31. Fischer, W. *et al.* Increase of intracellular Ca2+ by P2X and P2Y receptor-subtypes in cultured cortical astroglia of the rat. *Neuroscience* **160,** 767–783 (2009).

32. Marsault, R., Murgia, M., Pozzan, T. & Rizzuto, R. Domains of high Ca2+ beneath the plasma membrane of living A7r5 cells. *EMBO J.* **16,** 1575–1581 (1997).

33. Brini, M. *et al.* Transfected aequorin in the measurement of cytosolic Ca2+ concentration ([Ca2+]c): A critical evaluation. *J. Biol. Chem.* **270,** 9896–9903 (1995).

34. Montero, M. *et al.* Monitoring dynamic changes in free Ca2+ concentration in the endoplasmic reticulum of intact cells. *Embo J* **14,** 5467–5475 (1995).

35. Rizzuto, R., Simpson, A. W. M., Brini, M. & Pozzan, T. Rapid changes of mitochondrial Ca2+ revealed by specifically targeted recombinant aequorin. *Nature* **358,** 325–327 (1992).

36. Lim, D. *et al.* Calcium homeostasis and mitochondrial dysfunction in striatal neurons of Huntington disease. *J. Biol. Chem.* **283,** 5780–5789 (2008).

37. Lazzari, C. *et al.* Cellular prion protein is implicated in the regulation of local Ca2+ movements in cerebellar granule neurons. *J Neurochem* **116,** 881–890 (2011).

38. Kendall, J. M., Sala-Newby, G., Ghalaut, V., Dormer, R. L. & Cambell, A. K. Engineering the Ca2+-activated photoprotein aequorin with reduced affinity for calcium. *Biochem.*

Biophys. Res. Commun. **187,** 1091–1097 (1992).

39. Ramezani, A. & Hawley, R. G. Generation of HIV-1-based lentiviral vector particles. *Curr. Protoc. Mol. Biol.* **Chapter 16,** Unit 16.22 (2002).

40. Dagda, R. K. *et al.* Loss of PINK1 function promotes mitophagy through effects on oxidative stress and mitochondrial fission. *J. Biol. Chem.* **284,** 13843–13855 (2009).

5.6 Legends to Figures

Figure 1. Experimental setting for astrocyte culturing. Primary cultures of spinal astrocytes were isolated from hSOD1(WT) and hSOD1(G93A) newborn (P 0-1) mice and cultured for 3 weeks until cultures reached the confluence. Subsequently, they were re-plated at an optimal density (80.000 cells/well) in 24-well plates containing glass coverslips and maintained as described previously (Martorana *et al.* 2012; see also Materials and Methods). The day after plating, cells were transfected with the AAV9-cmv-cyt or AAV9-cmv-mt or AAV9-cmv-ER plasmidic vectors encoding the cameleon probes and used for experiments 72 h later. For cell transduction with the different AEQ isoforms, cells were infected with lentiviral particles (coding for AEQ_{pm}, AEQ_{cyt}, mt-AEQ_{mit} and AEQ_{ER}) 24 h after plating, and after further 72 h they were used for experiments. The same protocols for generation and culturing of spinal astrocytes was used for the measurement of mitochondrial membrane potential, WB and immunofluorescence analyses, and for mitochondrial morphology assessments.

Figure 2. **Primary cultures were almost pure in astrocytes and were efficiently transduced with the AEQ probes.** Panels A-C. 4 DIV primary spinal astrocytes were fixed and fluorescence immunostained with an antibody to the astrocytic marker GFAP (A, red signal), then counterstained with the dye Hoechst 33342 marking all nuclei (B, blue signal), and observed with a fluorescence microscope. Merge of the two images (C) and the below bar diagram, reporting the percentages of GFAP-negative (black bar) and -positive (red bar) cells, indicate that the astrocytic cultures did not suffer from significant contamination by other cell types. Panels D-E. Primary astrocytes transduced with a lentiviral vector coding for AEQ_{mit}, were immunostained for AEQ (D, green signal) and the astrocytic marker GFAP (E, red signal), indicating that the Ca^{2+} probe was effectively expressed in astrocytes. Data reported in the bar diagram are mean ± standard error of the mean (SEM), n = 45; ***$p < 0.001$, two-way Student's t-test. Scale bar = 50 μm in A-C; 20 μm in D-E.

Figure 3. Altered Ca^{2+} transients in fALS primary astrocytes compared to controls. hSOD1(WT) (black) or hSOD1(G93A) (red) primary spinal astrocytes were transduced with lentiviral vectors encoding AEQ_{PM} (A) or AEQ_{cyt} (B) targeted to sub-PM microdomains or bulk cytosol, respectively, and [Ca^{2+}] fluctuations after SOCE stimulation were recorded in such cell compartments. For SOCE stimulation, astrocytes were first incubated in a Ca^{2+}-free buffer containing EGTA (100 μM), and then perfused with $CaCl_2$ (1 mM), as indicated by arrows. The with-time average of the recorded traces is reported in left panels, while bar diagrams on the right report the peak values of Ca^{2+} transients. This data indicates that hSOD1(G93A) astrocytes have higher Ca^{2+} influx following SOCE than hSOD1(WT). Here and after, reported values are mean ±

SEM, numbers inside bars indicating the number of replicates (n). Peak values are: in PM microdomains, 19.97 ± 1.10 μM in hSOD1(G93A), 15.65 ± 1.11 μM in hSOD1(WT); in the cytosol, 1.40 ± 0.07 in hSOD1(G93A), 1.15 ± 0.03 μM in hSOD1(WT). ***p<0.001, two-way Student's t-test.

Figure 4. Higher ER Ca^{2+} refilling in fALS primary astrocytes compared to controls. hSOD1(WT) (black) or hSOD1(G93A) (red) primary spinal astrocytes were transduced with lentiviral vectors encoding AEQ_{ER} targeted to the ER, and ER Ca^{2+} replenishment was recorded following intracellular Ca^{2+} store depletion (by incubation in EGTA 500 μM and the Ca^{2+} ionophore ionomycin (5 μM), in a Ca^{2+}-free buffer) and subsequent SOCE activation (by treatment with $CaCl_2$ 1 mM), as indicated by arrows.The with-time average of the recorded traces reported in the left panel, and the bar diagram on the right reporting the ER peak values, indicate that ER Ca^{2+} uptake following SOCE is higher in hSOD1(G93A) than in control astrocytes. Peak values are: 338.47 ± 28.91 μM in hSOD1(G93A), 233.95 ± 16.61 μM in hSOD1(WT). Other experimental details are as in the legend to Figure 3.

Figure 5. No significant difference is observed in the expression of major SOCE-related proteins in astrocytes with the two hSOD1 genotype. Astrocyte lysates were analysed by Western blot for the expression of proteins belonging to the SOCE molecular machinery (i.e., ORAI1 and ORAI3, STIM1-2). In each panel, the upper figure reports a representative WB of the protein of interest (run at least in duplicate), while the lower bar diagram reports the densitometric analysis of immunoreactive bands normalized to the optical density of the corresponding Coomassie blue-stained lane, and reported as fraction of the mean value obtained with hSOD1(WT) astrocytes. No significant difference was observed in the expression of any of the analysed molecular SOCE components. Other experimental details are as in the legend to Figure 3.

Figure 6. hSOD1(G93A)-expressing astrocytes express comparable levels of ER stress-related proteins, but higher amounts of both SERCA and PMCA pumps. Protein extracts from astrocytes were analysed by Western blot for the expression of Ca^{2+}-dependent ER stress markers (i.e., calnexin (CLNX, panel A), calreticulin (CRT, panel B) and the unfolded protein response regulator GRP78, panel C) and of the sarco-endoplasmic reticulum and PM Ca^{2+} ATPases (SERCA and PMCA, panels D and E, respectively). While no significant difference was observed in the expression of ER stress-related proteins, both SERCA and PMCA were upregulated in fALS astrocytes compared to the healthy counterpart. ***p<0.001, two-way Student's t-test. Other experimental details are as in the legend to Figure 5.

Figure 7. No difference is observed in SOCE-evoked mitochondrial Ca^{2+} transients in primary astrocytes with different hSOD1 genotype. Ca^{2+} fluxes induced by SOCE were measured in hSOD1(WT) (black trace) or hSOD1(G93A) (red trace) by means of lentivirally-delivered AEQ_{mit}. Both the average traces reported on the right and the peak values reported in the bar diagram provide comparable results for the two astrocyte populations. Peak values are: 15.76 ± 1.38, hSOD1(G93A); 13.88 ± 1.09 μM in hSOD1(WT). Other experimental details are as in the legend to Figure 3.

Figure 8. No significant difference is observed in $\Delta\psi_m$ between fALS and healthy astrocytes. Primary astrocytes were loaded with the potentiometric fluoro-probe TMRM that is suited for comparing the mitochondrial membrane potential ($\Delta\psi_m$) between two populations of cells, whereby a decrease in TMRM fluorescence reflects mitochondrial depolarization. Representative images of TMRM-loaded astrocytes, before and after FCCP addition, are shown on the left panel, while the bar diagram on the right reports the quantitative fluorescence analysis (see Materials and Methods) indicating no difference in the mitochondrial polarisation between the two hSOD1 genotypes. Reported values are mean ± SEM; numbers inside bars indicate the number of coverslips.

Figure 9. No significant difference is observed in mitochondrial morphology between fALS and healthy astrocytes. Primary astrocytes were transfected with plasmidic vectors coding for a mitochondria-targeted red fluorescent protein (mtRFP), to assess mitochondria morphology/distribution by fluorescence microscopy. Representative fluorescence images of mtRFP-expressing astrocytes (72 h after transfection) are reported on the left, while the bar diagram on the right report the quantification of mitochondrial circularity (see Materials and Methods) showing no difference between the two hSOD1 genotypes. Other experimental details are as in the legend to Figure 8.

Figure 10. The Ca^{2+} channel-forming subunit of the mitochondrial Ca^{2+} uniporter (MCU) complex is equally expressed in astrocytes with the two SOD1 genotypes. Astrocyte lysates were analysed by Western blot for MCU expression, as shown in the upper representative WB of the protein (run in duplicate for each genotype), and the lower bar diagram reporting the densitometric analysis of MCU immunoreactive bands. Experimental details are as described in the legend to Figure 5.

Figure 11. Primary fALS astrocytes have higher ATP-evoked Ca^{2+} transients in the cytosol (but not in mitochondria) than the healthy counterpart. hSOD1(WT) (black) or hSOD1(G93A) (red) primary spinal astrocytes were transduced with lentiviral vectors encoding AEQ_{cyt} (panel A)

or AEQ_{mit} (panel B), and Ca^{2+} transients in the two cell compartments were measured following ATP stimulation in the absence of extracellular Ca^{2+}. To this purpose, cells were briefly (10 s) perfused with a Ca^{2+}-free, EGTA (100 mM)-containing buffer, and then treated with a Ca^{2+}-free solution containing ATP (100 μM). Under these conditions, ATP-evoked Ca^{2+} transients were specifically determined by Ca^{2+} release from intracellular (ER) stores. Such a stimulation protocol results in a higher cytosolic Ca^{2+} rise in hSOD1(G93A) astrocytes than in controls, as shown by the average traces of the left panel, and the Ca^{2+} peak values reported in the bar diagram on the right (A). Conversely, no difference is observable in mitochondria (B), suggesting that the organelles have a negligible role in the alterations of Ca^{2+} homeostasis induced by mutant hSOD1. Similar Ca^{2+} transients were observed when ATP stimulation was carried out in the presence of extracellular Ca^{2+} (1 mM), indicating that ionotropic purinergic receptors do not contribute to the observed Ca^{2+} mobilisation. Peak values are: 2.60 ± 0.05 μM in hSOD1(G93A); 1.98 ± 0.04 μM in hSOD1(WT), in the cytosol; 40.18 ± 2.95 μM in hSOD1(G93A); 38.92 ± 2.33 μM in hSOD1(WT), in the mitochondrial matrix. ***$p<0.001$ by two-way Student's t-test. Other experimental details are as in the legend to Figure 3.

Figure 12. Primary fALS astrocytes express much more P2Y6 receptor, but equal amounts of IP_3 or P2Y1 receptors, compared to control cells. 96 h from plating, astrocytes were collected and lysed, and protein extracts were subjected to Western blot analysis for the expression of IP_3R (A) or the purinergic metabotropic receptors P2Y6 (C) or P2Y1 (B). The upper part of each panel reports a representative WB of the protein of interest (run at least in duplicate for each hSOD1 genotype) and the corresponding Coomassie-stained lanes, while the lower bar diagram reports the densitometric analysis of immunoreactive bands. While no difference was observed for IP_3 and P2Y1 receptors, a significantly higher expression of P2Y6 receptors is evident in hSOD1(G93A) astrocytes compared to hSOD1(WT) cells. ***$p<0.001$, two-way Student's t-test. Other experimental details are as in the legend to Figure 5.

5.7 Figures

Figure 1.

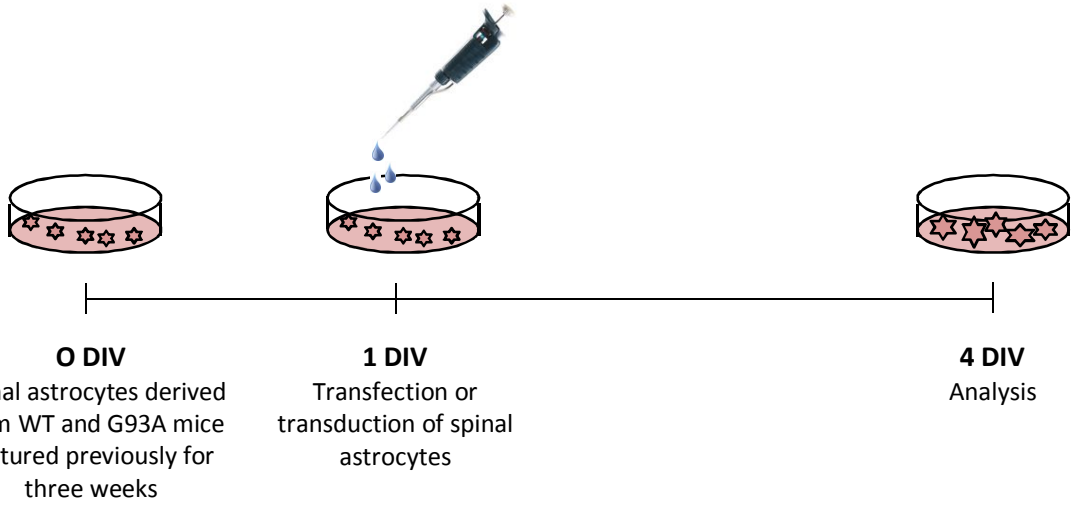

Figure 2.

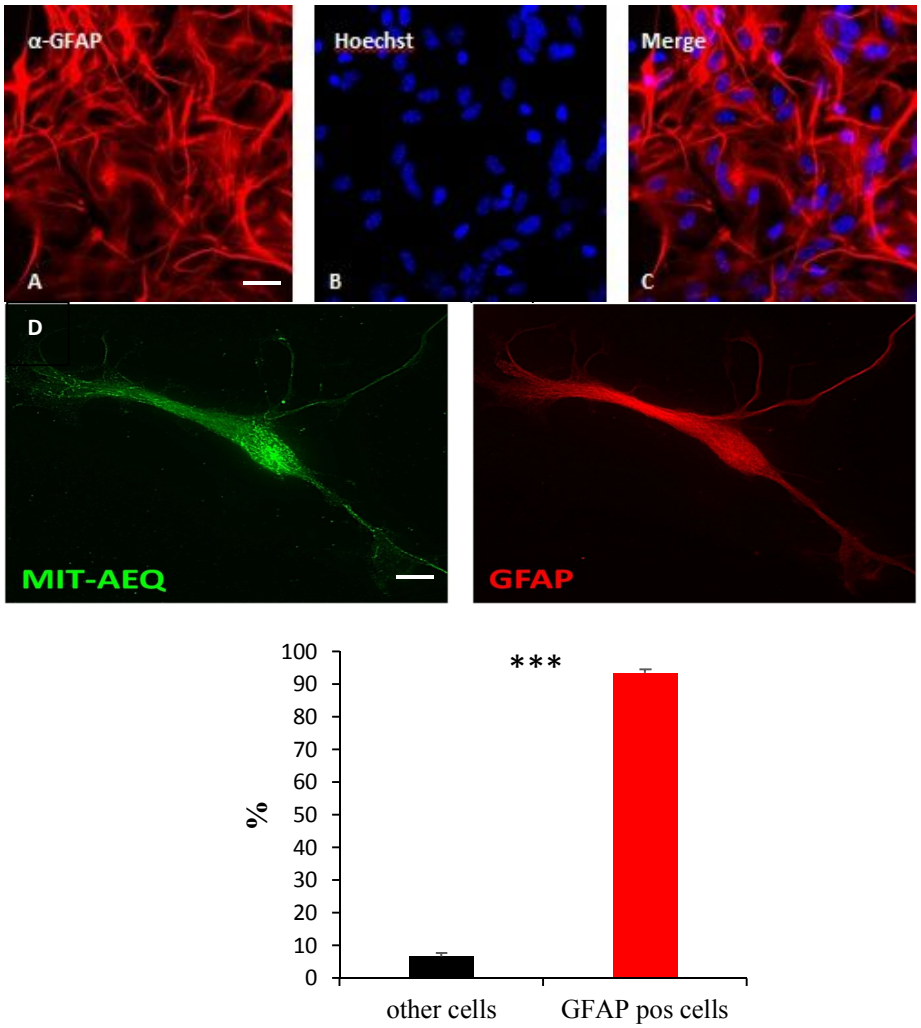

Figure 3.

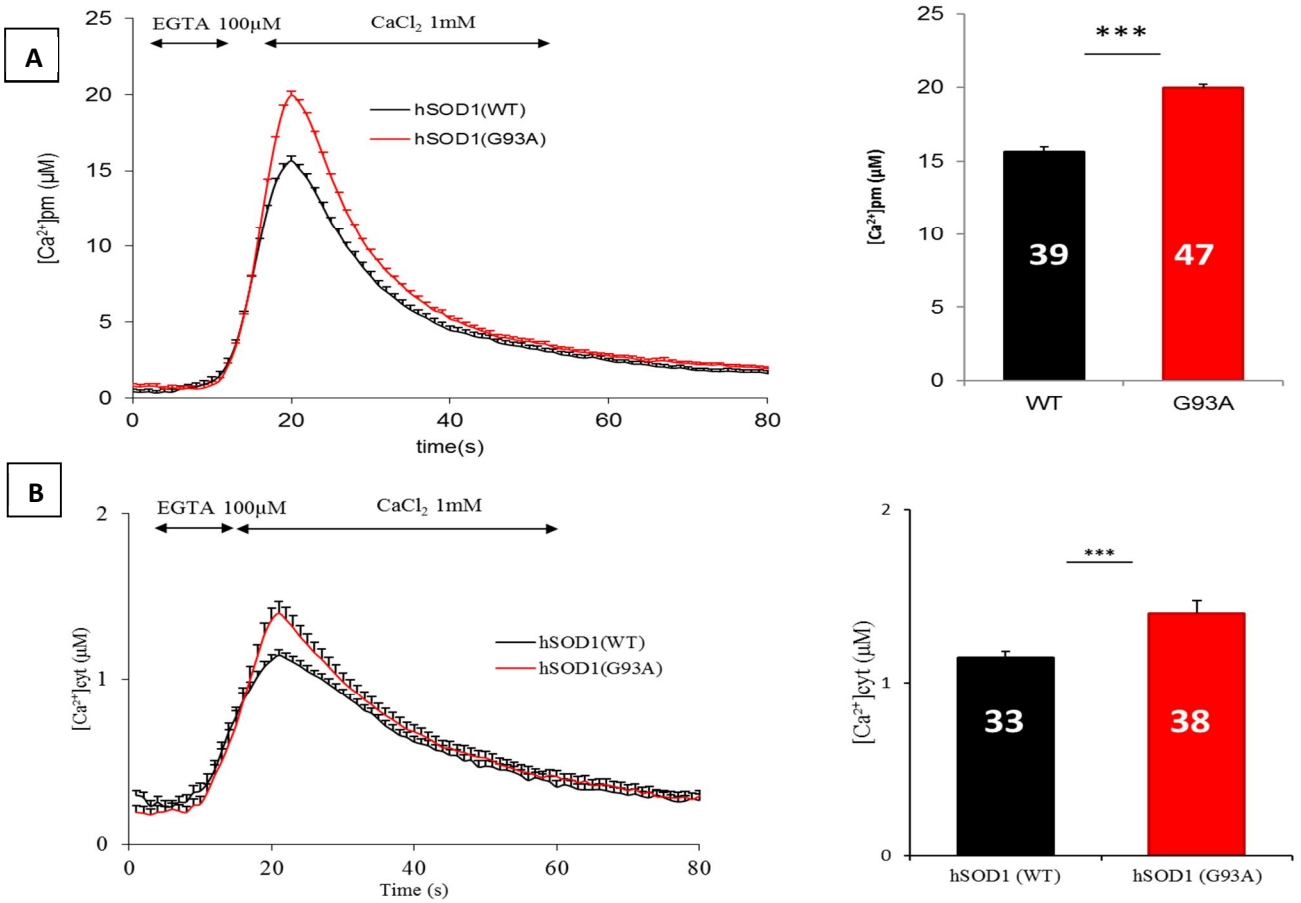

Figure 4.

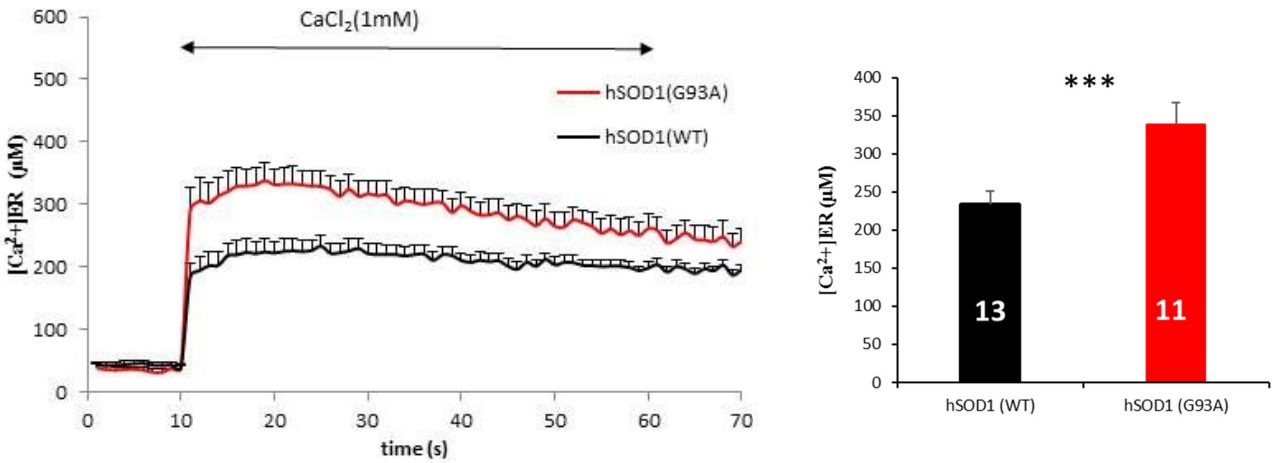

Figure 5.

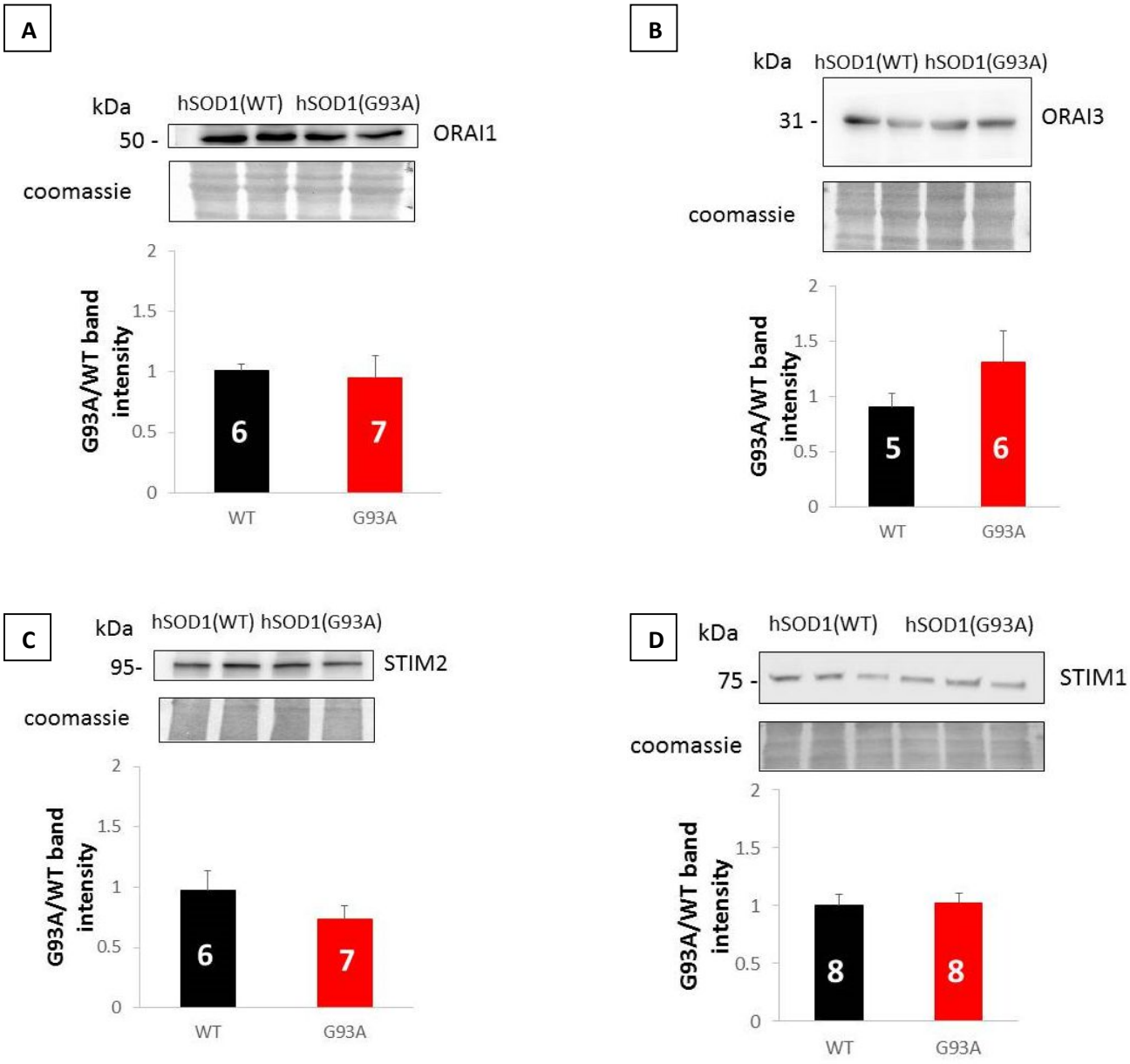
A
kDa
hSOD1(WT) hSOD1(G93A)
50 -
ORAI1
coomassie
G93A/WT band intensity
2
1.5
1
0.5
0
6
7
WT
G93A
B
kDa
hSOD1(WT) hSOD1(G93A)
31 -
ORAI3
coomassie
G93A/WT band intensity
2
1.5
1
0.5
0
5
6
WT
G93A
C
kDa
hSOD1(WT) hSOD1(G93A)
95-
STIM2
coomassie
G93A/WT band intensity
2
1.5
1
0.5
0
6
7
WT
G93A
D
kDa
hSOD1(WT)
hSOD1(G93A)
75 -
STIM1
coomassie
G93A/WT band intensity
2
1.5
1
0.5
0
8
8
WT
G93A

Figure 6.

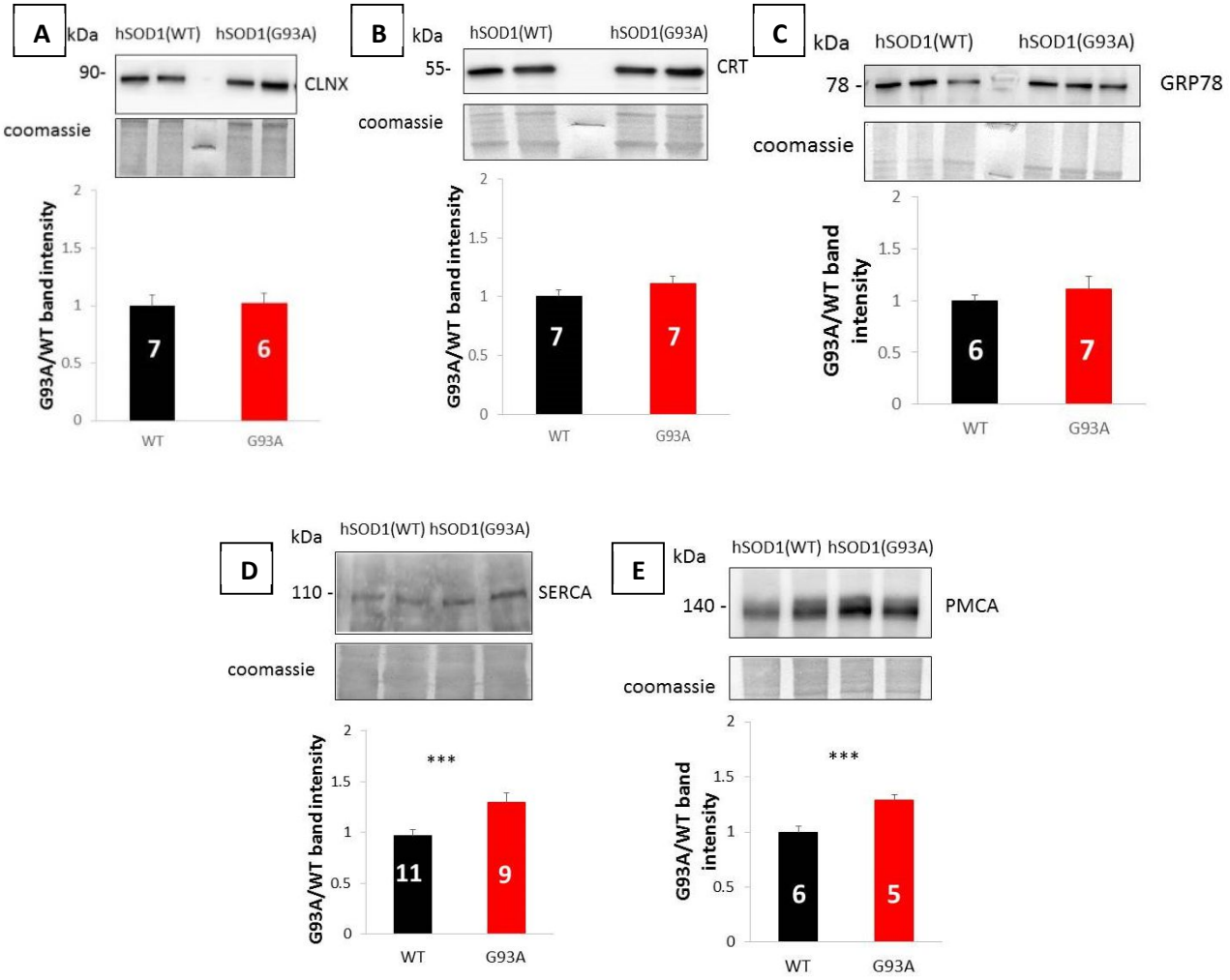

Figure 7.

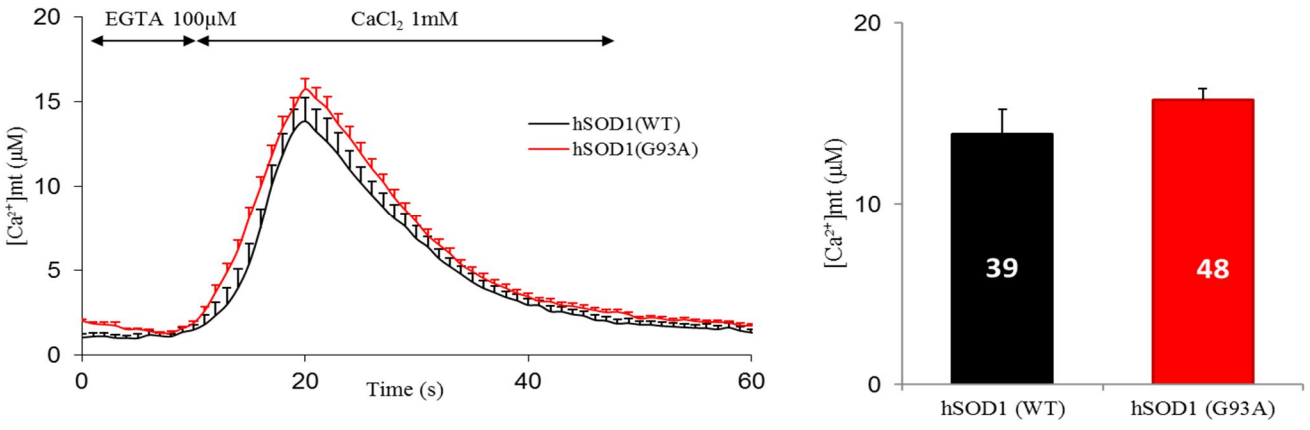

Figure 8.

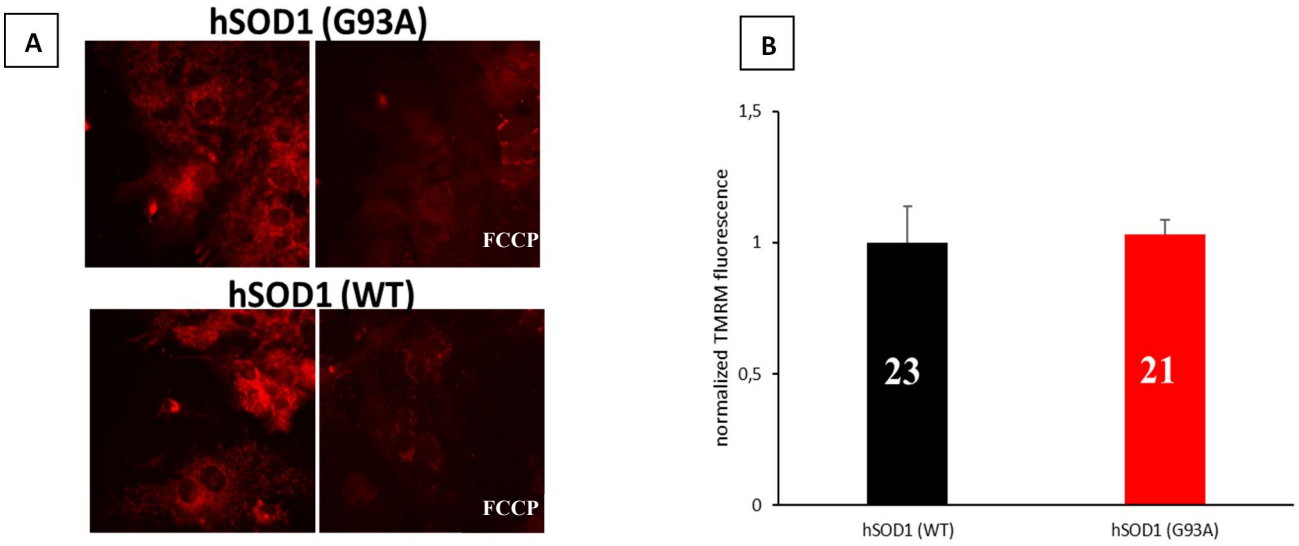

Figure 9.

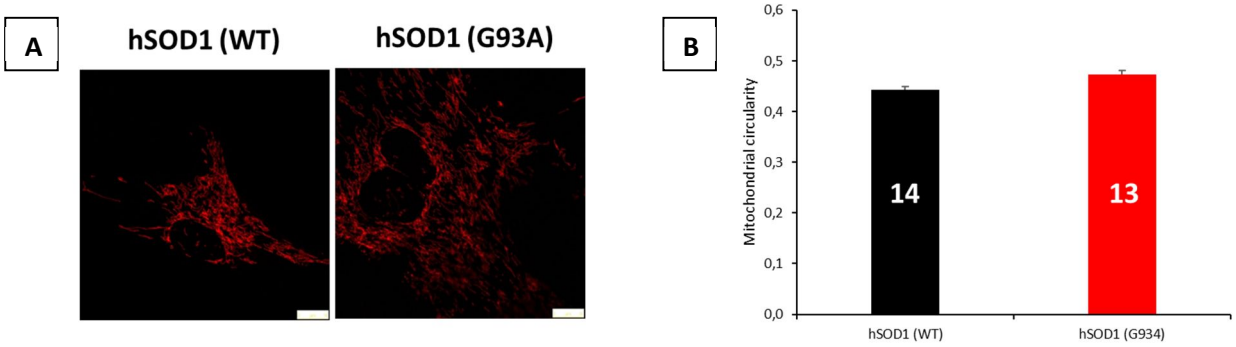

Figure 10.

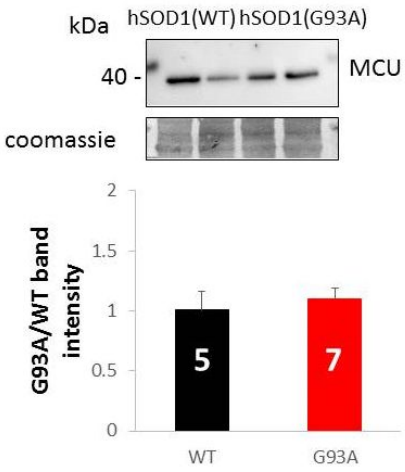

Figure 11.

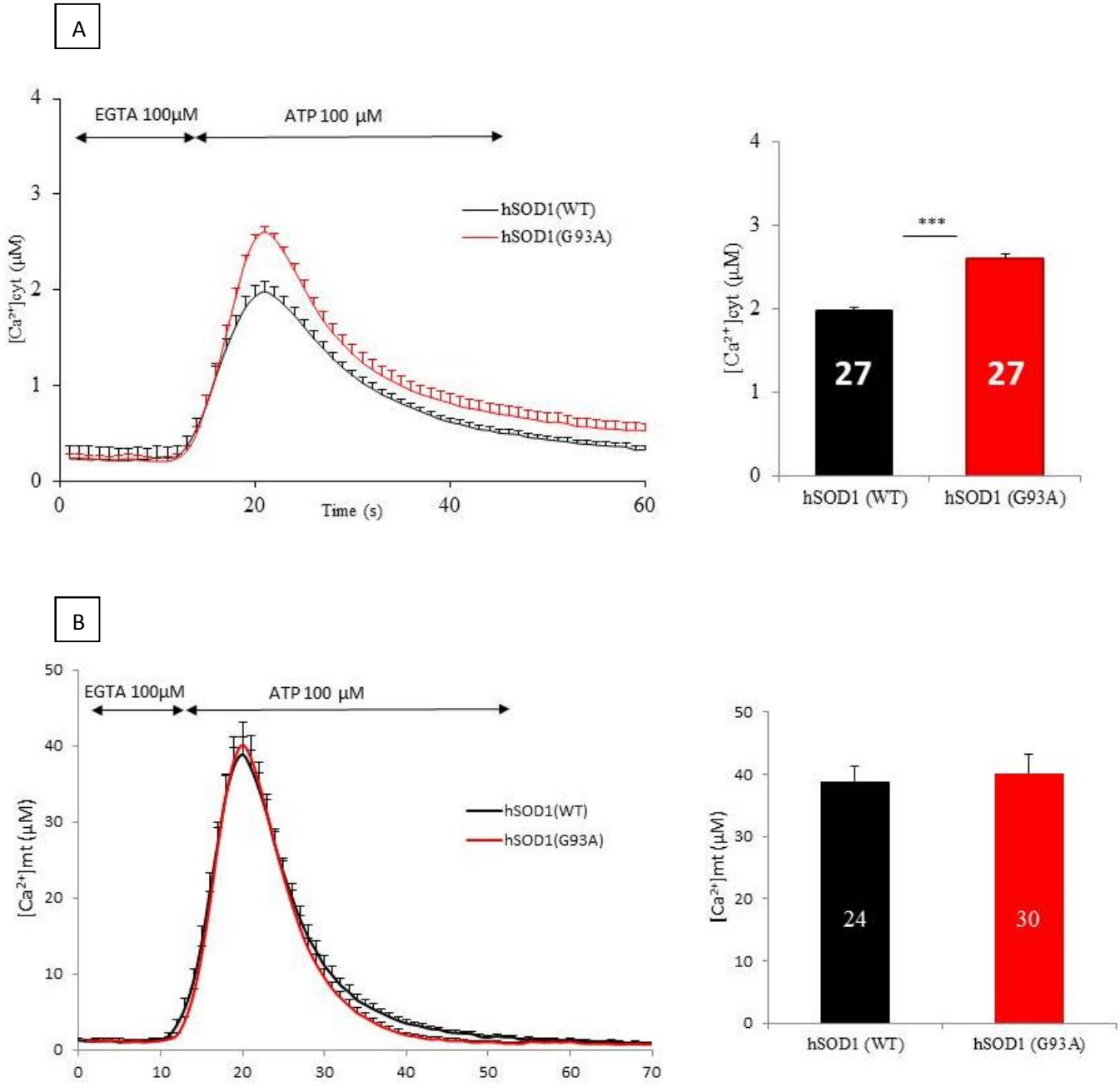
A
EGTA 100µM
ATP 100 µM
hSOD1(WT)
hSOD1(G93A)
[Ca2+]cyt (µM)
Time (s)
0
20
40
60
1
2
3
4
***
27
27
hSOD1 (WT)
hSOD1 (G93A)
B
EGTA 100µM
ATP 100 µM
hSOD1(WT)
hSOD1(G93A)
[Ca2+]mt (µM)
0
10
20
30
40
50
60
70
24
30
hSOD1 (WT)
hSOD1 (G93A)

Figure 12.

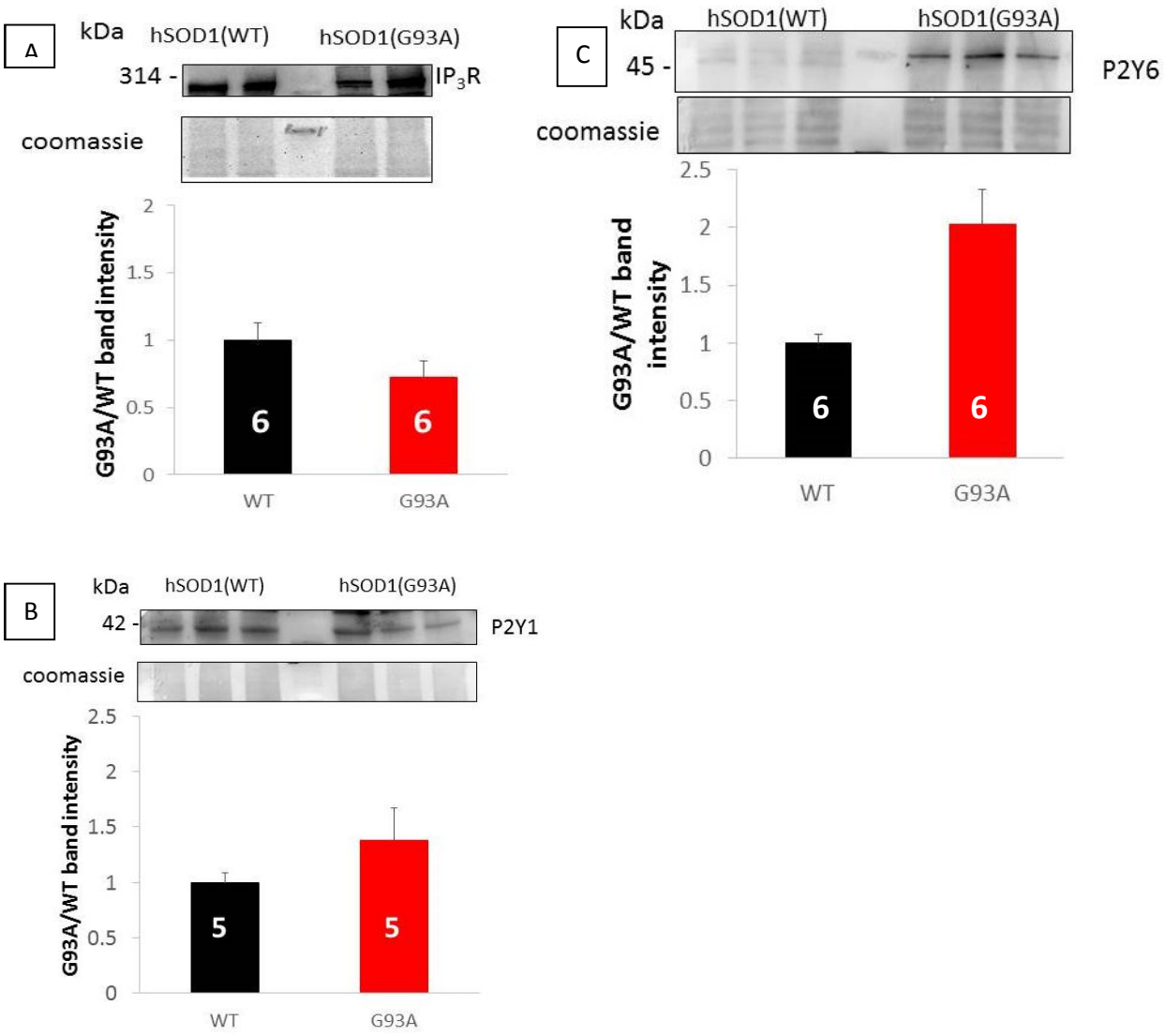
A
kDa
hSOD1(WT)
hSOD1(G93A)
314 -
IP3R
coomassie
G93A/WT band intensity
2
1.5
1
0.5
0
6
6
WT
G93A
C
kDa
hSOD1(WT)
hSOD1(G93A)
45 -
P2Y6
coomassie
G93A/WT band intensity
2.5
2
1.5
1
0.5
0
6
6
WT
G93A
B
kDa
hSOD1(WT)
hSOD1(G93A)
42 -
P2Y1
coomassie
G93A/WT band intensity
2.5
2
1.5
1
0.5
0
5
5
WT
G93A